Experimental analysis of coherent structures in a plane confined jet

by

Amitvikram Dutta

A thesis
presented to the University of Waterloo
in fulfillment of the
thesis requirement for the degree of
Master of Applied Science
in
Mechanical Engineering

Waterloo, Ontario, Canada, 2019

Author's Declaration

I hereby declare that I am the sole author of this thesis. This is a true copy of the thesis, including any required final revisions, as accepted by my examiners.

I understand that my thesis may be made electronically available to the public.

Abstract

Confined jets are commonly employed in several industrial applications such as propulsion systems in the aerospace industry and environmental control systems. In the present study, the flow development of a high aspect ratio, planar confined jet is studied. The velocity field is measured using time-resolved, two-component, Particle Image Velocimetry. The study focuses on the differences in flow development with respect to coherent structures formed in the jet shear layer between an unconfined jet and a confined jet at two confinement ratios (CR) of 7 and 5. All three cases were investigated at a Reynolds number of 3800 based on jet exit height and centreline velocity. For all cases examined, primary vortices form downstream of the jet exit, due to the amplification of perturbations in the shear layer. The Strouhal number corresponding to the initial vortex shedding frequency is relatively unchanged between the confined and unconfined cases at around $St_0 = 0.67$. The perturbations associated with this non-dimensional frequency grow exponentially downstream, saturate and then decay. For the unconfined case, this saturation takes place at 1.8 jet slot heights (h) downstream. For the confined cases, the spatial growth rate of fluctuations is lower, and the perturbations saturate at $3.1h$ and $3.7h$ for the CR = 7 and CR = 5 cases, respectively. These locations of saturation also correspond to the locations of onset of growth of perturbations associated with the subharmonic ($St_0/2$). The subharmonic corresponds to the passage frequency of structures formed from the pairing of primary vortices. Therefore, for the confined cases, the location of pairing of the initially shed vortices is shifted further downstream. The primary structures for the unconfined case are seen to be convected at 57% of the jet centreline velocity, while for the confined cases this increases to an average convective velocity of 63% of the jet centreline velocity. The characteristic wavelengths of the primary structures for the unconfined case was found to be $0.8h$ while for the two confined cases this increases to $1.1h$. Proper Orthogonal Decomposition (POD) analysis showed that for the unconfined case, within the first 5 slot jet heights, the most energetic mode pair corresponds to coherent structures which have undergone two complete pairings, while for the confined cases, the most energetic mode pair corresponds to primary vortices.

Acknowledgements

I would like to thank my supervisors Dr. Serhiy Yarusevych and Dr. Jean-Pierre Hickey for their invaluable help and guidance in all aspects of this masters research project. Without their oversight and comments, this work would not have been possible.

I would also like to thank my colleagues in the Fluid Mechanics Research Lab (FMRL) and Multi-Physics Interaction Lab (MPIL) who added greatly to my understanding of the various aspects of fluid mechanics through several illuminating discussions.

I'd like to thank Burak Ahmet Tuna for his close collaboration during the project and for effectively collecting and providing the data that was utilised.

Thank you Prarthana, for your unwavering emotional and mental support, which proved to be just as important as those of other forms.

Finally, I would like to thank my mother, a person who shows me every day, how not to give up.

Table of Contents

List of Tables

List of Figures

Nomenclature

$< \hat{v} >$ Root-Mean-Square of frequency filtered streamnormal fluctuations

CR Confinement ratio (H/h)

D Diameter of jet exit for axisymmetric jet

H Height of confinement box

R Velocity ratio of shear layer

RSS Reynolds Shear Stress

Re Jet exit Reynolds Number

St Strouhal number

St_0 Shedding frequencies of primary structures

U Mean velocity

U_0 Centreline velocity at the jet exit

U_{cv} Convective velocity of coherent structures

U_c Local jet centreline velocity

α_i Complex wavenumber of disturbance fluctuations

λ_2 Lambda 2 criterion for identifying coherent structures

λ_i Eigenvalues from POD analysis

λ_{x0} Streamwise wavelength of primary structures

λ_x Streamwise wavelength of coherent structures

ν Kinematic viscosity

ω_c Vorticity

ψ_v Streamnormal component of eigenmodes from POD analysis

$\vec{\psi_i}$ Eigenmodes from POD analysis

$\vec{u'}$ Reconstructed velocity field from POD

a_i Temporal coefficients from POD analysis

$f_\#$ Numerical Aperture

f_{ac} Acquisition frequency for time-resolved data

f_n Fundamental frequency of the shear layer

h Slot height of jet exit for a planar jet

k Streamwise wavenumber of coherent structures

r Radius of jet exit for axisymmetric jet

u' Streamwise velocity fluctuations

u_{rms} Root-mean-square of streamwise fluctuations

$v^{'}$ Streamnormal velocity fluctuations

v_{rms} Root-mean-square of streamnormal fluctuations

x Streamwise coordinate along jet centreline

y Streamnormal coordinate normal to jet centreline

$y_{0.5}$ Local jet half-width

z Spanwise coordinate normal to jet centreline

Chapter 1

Introduction

Jet flows are characterised by a source of momentum flux into stationary or moving fluid with lower momentum. A characteristic feature of such flows is the presence of shear layers. Shear layers develop when a velocity gradient exists between two fluid flows. In jet flows as the source fluid with higher momentum discharges into the nearly stagnant ambient fluid, a shear layer is formed along the boundary of the two flows. Planar jets are a sub-class of such flows where the flow exiting the jet exit is two dimensional in the mean sense. They are characterized by two shear layers on either side of the centreline and the flow develops as these layers entrain the surrounding fluid. Confined jet flows occur when, downstream of the jet exit, the flow is constrained by walls in the streamnormal direction. Such confinement causes significant changes in the nature of the entrainment and thus the overall nature of flow development as compared to unconfined jets [1, 2].

Planar jets in both confined and unconfined forms find widespread industrial uses. In the aerospace industry, they are used in propulsion and lift augmentation systems [3]. They have also found use in applications related to environmental control, e.g. Air-Curtains [4] and HVAC (Heating Ventilation and Air-Conditioning) [5]. Oil drilling and storage

operations use confined jet flows extensively [6], and, in manufacturing operations, high temperature furnaces make use of confined jets in order to enhance their heat-transfer properties and for better flame control [7].

The shear layers in plane jets feature organized flow regions that are termed as coherent structures [8, 9]. These structures are formed due to the Kelvin-Helmholtz instability of the shear layers downstream of the jet exit [10, 11]. The instability leads to the amplifications of fluctuations and as the fluctuations reach their maximum amplitude the shear layer rolls up to form the coherent structures which are shed periodically. In plane jet flows these structures take the form of long spanwise rollers with the vortex cores extending along the entire length of the structures [12]. These structures then grow by entraining the ambient fluid and can pair downstream due to mutual induction. The growth of the jet and thereby is overall flow development is governed by the pairing of these structures The shedding and pairing frequencies are dependent on the mean flow and background perturbation characteristics [9, 10]. The coherent structures are convected along the shear layers and continue to grow and pair until they eventually break-down far downstream.[13].

Over the last decade, the introduction of advanced experimental techniques, such as Particle Image Velocimetry (PIV), have allowed the measurement of entire velocity fields, which has, in turn, contributed significantly to the understanding of coherent structures and their role in the shear layer [14]. PIV allows the capture of both temporal and spatially resolved velocity fields in sufficient detail which is crucial for the analysis of the behavior of these structures and the effect of various conditions on their development.

While the mean and turbulent properties of confined jets downstream of the the potential core have been extensively studied by analytical, experimental, and computational methods [1, 2, 15, 16, 17, 18], the effects of confinement on initially laminar shear layers and the coherent structures formed close to the jet exit have received relatively little at-

tention. Therefore, there exists a knowledge gap regarding the development of coherent structures in confined plane jets. A better understanding of the behavior of these structures under confined conditions could be useful in designing more efficient furnaces and other burner applications in manufacturing industries [19]. As these structures are crucial in the characteristics and development of the jet, the effects of confinement on them is a question of significant interest. In the present study, the near field of a high-aspect ratio plane jet is experimentally investigated using time-resolved PIV, with particular emphasis on the behavior of coherent structures. The main objective of the study is as follows:

- Characterize the effects of confinement on the behavior of coherent structures in a plane jet flow.

The study is presented in the following format in this thesis. A literature review covering general features of unconfined jets, confined jets, and coherent structures in jet flows is provided in Chapter 2. Chapter 3, describes the experimental setup. The results of the study and their accompanying analysis is presented in Chapter 4, with a summary of the conclusions detailed in Chapter 5 and recommendations given in Chapter 6.

Chapter 2

Literature Review

2.1 Properties of Unconfined Jet Flows

Unconfined or free jet flows are characterised by three distinct regions as shown in Figure 2.1. As the fluid issues from the jet exit, the flow field is initially characterised by a region of uniform mean velocity along the centreline. This region is termed as the potential core, the velocity gradient between the high-momentum potential core and the lower-momentum ambient gives rise to a shear layer. Axisymmetric free jets have a single shear layer while planar jets feature two shear layers on either side of the centreline. The shear layer(s) grow as they entrain the ambient fluid and eventually they meet at the end of the potential core which extends upto 6 to 8 jet diameters (r) for axisymmetric jets [20, 21] and 4 to 7 jet slot heights (h) for planar jets [22, 23]. Downstream of this region, the scaled values of the local centreline velocity (U_c) decays with streamwise distance (x) as $U_c \propto x^{-0.5}$. The local jet half width ($y_{0.5}$) is defined as the distance from the jet axis in the streamnormal direction, where the local velocity is half of the centreline velocity. In this region, the jet half-width grows linearly as $y_{0.5} \propto x$ [24]. In this decay region which extends up-to 15 - 20

h the plane jet transitions to the far-field Gaussian profile shape [25]. The lengths of the

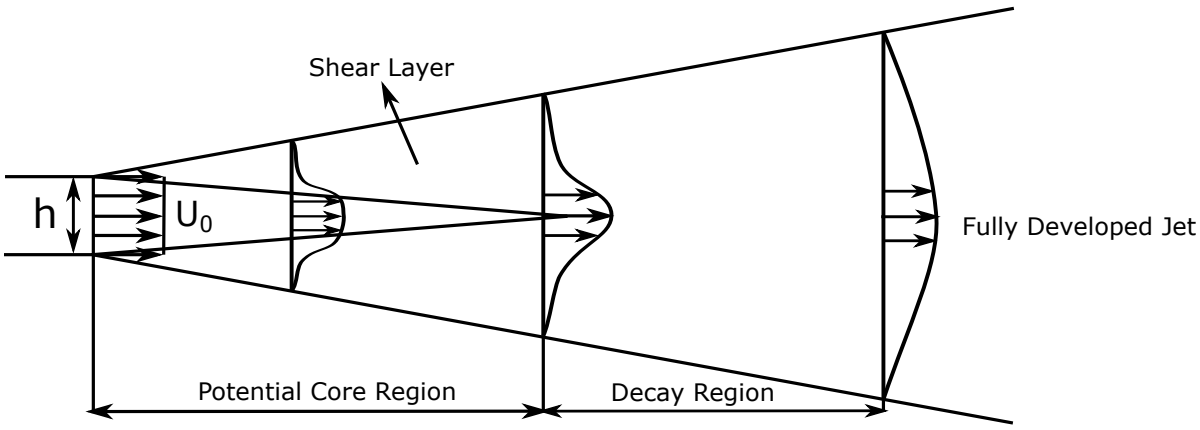

Figure 2.1: Free Jet Flow

potential core and the transition region depend on the jet exit Reynolds number defined as

$$Re = U_0 h/\nu \tag{2.1}$$

where U_c is the area averaged exit velocity and h is the jet exit slot height (Jet exit radius (r) for axisymmetric jets). Deo et. al. [25], conducted experiments with plane jets with Re up to 25,000 and observed that an increase in Re causes the length of the potential core to decrease and points to an increase in the near-field jet spreading rate. On the other hand, the far-field jet spreading rate shows the the opposite dependence on Re. It decreases asymptotically with increase in Re, with a comparable rate of convergence to that in the near field. The turbulence statistics in the jet flow field are also highly dependent on Reynolds number for $Re < 25{,}000$. Mi et. al. [26] were the first to show that the local maxima of the magnitude of turbulent intensity in the near field depends on initial conditions of the jet flow. Deo et. al. [25] determined that the magnitude of the initial turbulence intensity peak decreased and its streamwise location moved upstream with increasing Reynolds number from 1500 to 16,500, from which it was deduced that

this local maximum was associated with the primary vortex formation. However, the asymptotic value of the far-field intensity shows an opposite dependence and increases with an increase in Re [25].

The near field dynamics of jet flows is dominated by coherent structures [9]. These structures arise due the susceptibility of the shear layer to perturbations through the Kelvin-Helmholtz instability mechanism [27]. In plane jets, coherent structures take the form of counter-rotating spanwise vortices which form on the opposite side of the jet due to the roll up of the shear layers. The existence of these structures was verified by Antonia et. al.[28] by spatio-temporal correlation of hot-wire measurements. They determined that, close to the jet exit, the structures are arranged symmetrically about the centre-line of the jet, while downstream of the end of the potential core these structures rearrange into an asymmetric alignment. These conclusions were farther verified by the work of Thomas and Goldschmit [29] who used measurements of energy content of velocity fluctuations to infer the existence of symmetrical structures exhibiting two-dimensionality in the spanwise direction close to the jet exit. Browne et.al. [29] showed that, beyond the end of the potential core, the dramatic redistribution of turbulence quantities is associated with the loss of this spanwise coherence. The large scale structures were found to be convected at approximately 60% of the local centreline mean velocity [30], [31] and [32].

The shape of the profile of the mean velocity at the jet exit was found to have a significant effect on the arrangement of the coherent structures. Jets with nearly uniform or 'top-hat' exit velocity profiles were found to give rise to the aforementioned symmetrical arrangement of coherent structures [33, 34]. A parabolic profile, such as that at the exit of a long pipe, leads to structures where the anti-symmetric mode dominates about the centre-line [35, 36].

The coherent structures in the shear layer are responsible for the entertainment of and

transfer of momentum to the fluid surrounding the jet. This results in the widening of the shear layers and thus spreading of the jet. As the structures move downstream, they grow larger and interact with each other. This interaction takes the form of merging of adjacent vortices [12, 34]. Winant and Brownand [10] demonstrated experimentally that the successive pairing of vortices was the primary mode of mixing layer growth. Experimental observations have verified this with several studies [37, 23, 38, 36, 39] of plane and axisymmetric jets. In these studies, cross stream RSS profiles at several successive axial locations downstream showed maxima in the shear layer regions where the flow is dominated by vortices. Profiles of other turbulent quantities, namely, the root-mean-squared magnitudes of streamwise and streamnormal fluctuation velocities also reached their peak values in the shear layer.

Additional insight into the formation and evolution of coherent structures in shear layers may be obtained from stability theory as coherent structures are manifestations of hydrodynamic instabilities [40]. Michalke [41] conducted a comprehensive study on temporal and spatially growing instabilities in a hyperbolic-tangent velocity profile. This study confirmed the validity of linear stability theory to the study of disturbances in the shear layer. Monkewitz and Huerre [42] studied the effects of the ratio of velocities of the two streams of the shear-layer on the characteristics of spatially growing disturbances for the hyperbolic tangent profile. The non - dimensional frequency or Strouhal number corresponding to the most amplified disturbances ($St = 0.032$) corresponded to the natural frequency of the shear layer. It was found to be weakly dependent on R -(the velocity ratio of the shear layer), varying only 5% between R = 0 (wake-flow) and R = 1 (single fluid).

Ho and Huang [43] proposed a subharmonic model for the evolution of instabilities in the shear layer. It suggests that the coherent structures are formed from the initial instability at the fundamental frequency of the shear layer (f_n). As the instabilities grow and evolve

downstream, their energy content reaches a maximum. Thereafter, the first subharmonic ($fn/2$) starts to grow and becomes the most amplified instability. This subharmonic was seen to be saturated at the physical location where two vortices merged and the second subharmonic ($fn/4$) started to grow. Thus, the initial vorticity is constantly redistributed into larger vortices while the frequency is halved at each pairing.

Monekwitz [44] suggested that in the presence of natural or artificial broadband forcing of a shear layer there exists a detuning parameter that modulates the subharmonic modes at an approximate frequency of $\pm 0.08 f_n$. The applicability of this subharmonic evolution model to the near field of plane jets was demonstrated by the experiments of Hsaio and Huang [45].

Thomas and Chu [45] and Thomas and Prakash [36] conducted experimental studies of plane jets with low level artificial forcing. They found that at downstream locations spectral sideband frequencies $f_n/2 + / - f_c/2$ arose, where the modulation frequency of $f_c/2$ corresponded exactly to the detuning parameter of $0.08 f_n$ proposed by Monkewitz [44].

2.2 Confined and Co-flowing Jets

Confined jets refer to a particular class of flows where the spread of the primary jet stream is confined along a particular axis. For axisymmetric jets, this is achieved by a coaxial wall placed symmetrically downstream of the jet exit. For plane jets, confining walls are usually placed normal to the axis of mean jet flow. Fully confined jets, i.e. jets with no co-flow streams develop in a manner shown in Figure 2.2. Downstream of the jet exit, large recirculation regions develop on either side of the centreline and close to the jet exit. As in unconfined jets, shear layers develop along the boundary between the primary flow and the recirculation region. In contrast to unconfined jets however, the length of the potential

core is shorter and the centreline velocity of the jet decays more rapidly after its end [46]. This is accompanied by the spread of the jet due to the shear layer between the bulk flow and recirculation regions. The point at which the flow spreads to the walls marks the end of Region 1. Thereafter, the flow continues as normal pipe or channel flow [47]. More detailed descriptions of fully confined jets may be found in the following studies [48, 49].

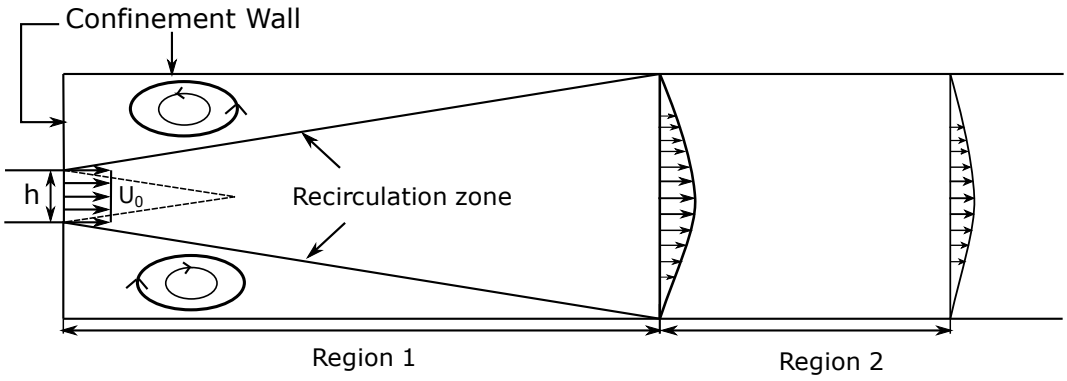

Figure 2.2: Confined jet with no co-flow

Figure 2.3 gives an overview of the different flow regions of a confined jet with a parallel co-flowing stream present. Downstream of the jet exit in Region 1 the flow is characterized by the presence of a potential core similar to that of an unconfined jet, with the jet centreline velocity remaining constant in this section. However, due to the presence of the co-flow, recirculation zones do not form in this region. Instead, shear layers form between the primary stream and the co-flow due to the velocity gradient present at the interface. These shear layers grow downstream and meet at the end of the potential core at the end of Region 1. Downstream of this region, depending on flow conditions present, a recirculating zone is formed at the confining wall in Region 3. Beyond Region 3 the flow develops eventually to fully developed pipe flow. In a broad qualitative sense if unconfined jets and fully confined jets with no co-flow represent two extremes, confined jets with co-flows show characteristics which lie between the features of these marginal cases. For

brevity, confined jets with co-flows, which form the principal topic of this work are hereafter referred to as confined jets.

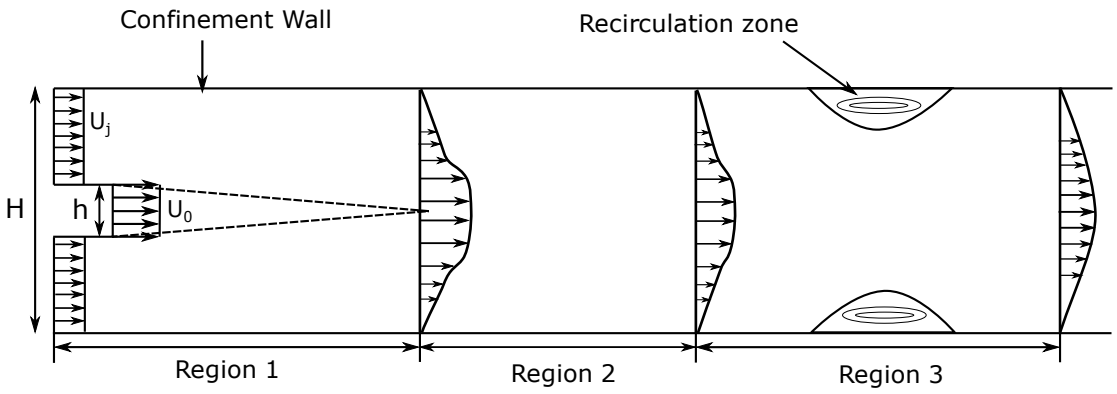

Figure 2.3: Confined jet flow

The mean flow characteristics of the confined jets were found to be broadly similar to unconfined jets in terms of centreline decay and jet spread rate [50]. Downstream of the potential core the centreline velocity for plane confined jets was found to decay as $U_c \propto x^{-0.5}$ [2] while the jet spread rate was linear as $y_{0.5} \propto x$ [1]. These relationships are identical to those for an unconfined planar jet and were valid for Region 2 of the confined jet i.e. downstream of the end of the potential core and upstream of the recirculation zone. However, the actual centreline decay and jet spread rate were found to be smaller in the case of confined jets with co-flows than for unconfined jets with similar jet exit conditions. Additionally, the rates of growth and decay and the length of the potential core were found to be dependent on the ratio (R) between the main jet flow and the co-flow rate. Curtet [2] and Hill [50] determined that decreasing the ratio of the co-flow to the primary flow caused a decrease in the potential core length and an increase in the centreline velocity decay and jet spread rate respectively for both axisymmetric and plane confined jets. Razinsky and Brighton [15] studied confined axisymmetric jets at high Reynolds Numbers (52000 - 295000) under conditions where no recirculation bubble was present in the flow. Two sets

of data were obtained with co-flow velocity to main jet velocity ratios (R) of 0.5 and 0.1. Cross stream profiles of Reynolds Shear Stress (RSS) showed a maxima at the shear layer as in unconfined jets [15]. Additionally, an increase in R showed a decrease in the peak RSS magnitude in the shear layer. This relation was also confirmed in a study by Habib and Whitelaw [51] for different values of R. Antonia and Bilger [16], investigated the far-field turbulent characteristics of an axisymmetric jet discharging into a variable co-flowing stream.Two sets of data were obtained with co-flow velocity to main jet velocity ratios (R) of 0.333 and 0.222. They found that, while the profiles of RMS of streamwise and radial velocity fluctuations and the RSS for axisymmetric jets collapse in the far-field ($x/D > 50$), in the presence of co-flow no such collapse was observed. These results were confirmed by Yule and Damou [17] who studied the variation of turbulent quantities of co-flowing jets at small values of R (0.033, 0.077, 0.17), at large downstream distances ($x/D > 30$). They observed that, unlike free jets, the far-field turbulence intensity continued to increase till the end of the experimental domain and did not asymptote to a value thereby indicating that the jet was still in its developing phase. An explanation for this strong dependence on jet exit conditions is provided in [16], where it is stated that the turbulent kinetic energy budget has a strong advective component and thus the effects of the jet exit conditions persist far downstream.

The effects of confinement on the coherent structures in jets have received relatively little attention in literature. Nickels and Perry [52] investigated turbulent axisymmetric co-flowing jets under differing co-flow ratios ($R = 0.05, 0.1, 0.5$) using hot-wire and pitot-static measurements. They concluded that the overall structure of the jet consists of large scale structures which scale with local jet width. Evidence of smaller structures which were isotropic in nature was also obtained but these were not conclusive. A more quantitative study of the coherent structures in confined jets was undertaken by Kong *et. al.* [53].

Measurements of the near-field of a confined planar jet with co-flow were obtained using PIV and the swirling strength of the vortices was employed as their defining characteristic. The vector fields obtained showed the presence of a small wake region between the jet and the co-flow close to the jet axis and the development of counter-rotating structures similar to those in free-jets. These structures were seen to be spindle-shaped with a titling stream-wise major axis.

The effect of a co-flow and the wake generated by thickness of the nozzle lip walls on the inviscid instability characteristics of a jet was first described by Michalke [54]. In this investigation, two possible modes of instability were determined, the so called "wake" mode and "jet" mode. Talamelli and Gavarini [55] then determined that for certain values of duct shear layer thicknesses and velocity ratios, the wake mode developed an absolute instability, with its frequency of the instability being almost constant if normalised by velocity and shear layer thickness. Segalini and Tamalelli [56] carried out an experimental analysis of dominant instability modes in the near field of coaxial jets. They focused on the critical parameter of the velocity ratio (R) and showed that for values of $R < 0.75$ the dynamics of the coaxial jet are determined by the inner shear layer, while for $R > 1.6$ the outer shear layer is of greater importance in the near field.

However, while the importance of the conditions at the jet nozzle exit on the far-field behavior of confined jets has been noted in previous studies, the behavior of these flows in the near-field, close to the jet exit, has remained relatively unexplored. The study of confined jets has largely been limited to the prediction of the formation of the recirculation bubble and the flow field further downstream. The effect of confinement on coherent structures has received relatively little attention in the literature. This is the gap that the present work aims to address.

Chapter 3

Experimental Methodology

In the present study, the effects of confinement on the development of the near field of a plane air jet are investigated experimentally. Flow field measurements are conducted for three different cases, namely, one unconfined case and two confined cases with confinement ratios (CR) of 7 and 5. The confinement ratios are defined as the ratio of the height separating the confinement surfaces in the streamnormal direction *(H)* and the jet exit height *(h)* as shown in Figure 3.3. Particle Image Velocimetry (PIV) is used to characterize the flow-field and the coherent structures that are of interest. The description of the experimental setup used for this investigation is given in this chapter.

3.1 Experimental Setup

The overall arrangement of the experimental setup is show in Figure 3.1. The air for the jet is supplied by a regenerative type blower which is controlled by an Allen-Bradley variable frequency drive. An additional valve is installed at the blower intake as a throttle to control

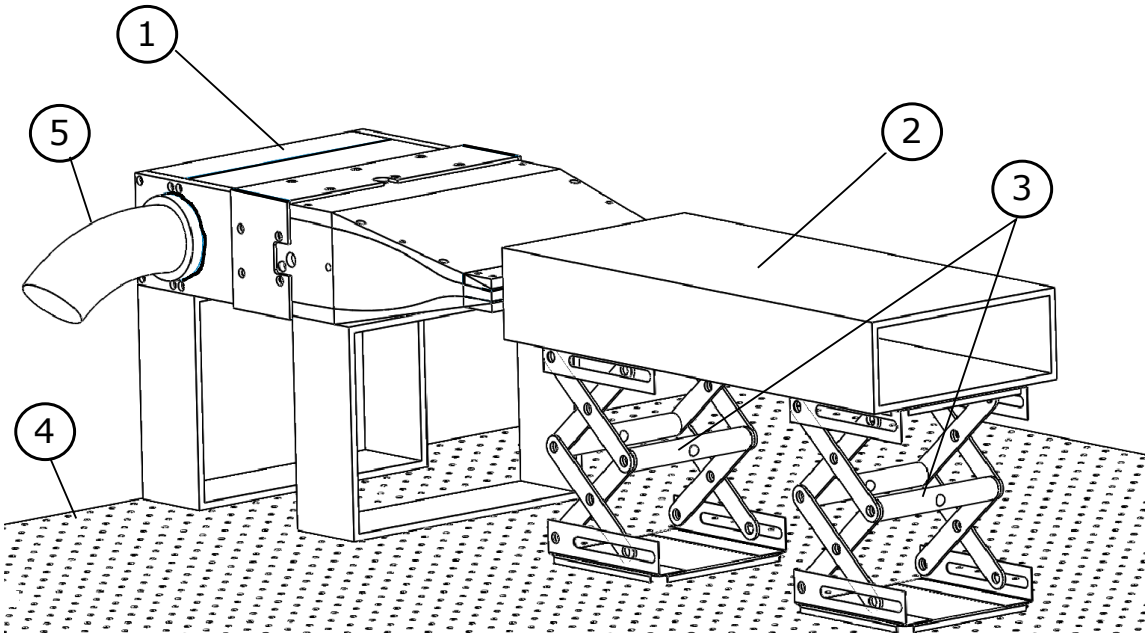

Figure 3.1: Experimental Setup: 1. Plane jet nozzle assembly 2. Transparent confinement box 3. Lab Jack supporting confinement box 4. Optical table 5. Flexible hose to air-supply

the flow rate independently of rotation speed. The blower was operated at a constant speed to ensure identical jet exit velocity and hence Reynolds number for all cases. The air from the blower is supplied to the jet nozzle assembly using a flexible hose.

The plane jet nozzle assembly consists of a plenum and settling chamber which contains flow conditioning elements and contoured profile section that forms a planar jet. The flow from the blower is first routed into a flow distribution tube as shown in Figure 3.2. The tube has three sets of azimuthal holes with varying diameters along its span and a separation angle of 60^o, which are aimed at the top of the plenum marked as (1) in Figure 3.2. The top of the plenum is shaped as a half cylinder, coaxial to the flow distribution tube. This configuration of the tube allows the flow to be directed towards the settling chamber after mixing. Downstream of the distribution tube, flow uniformity and reduction of velocity fluctuations is ensured by a honeycomb screen (5) and four mesh screens (6) that are

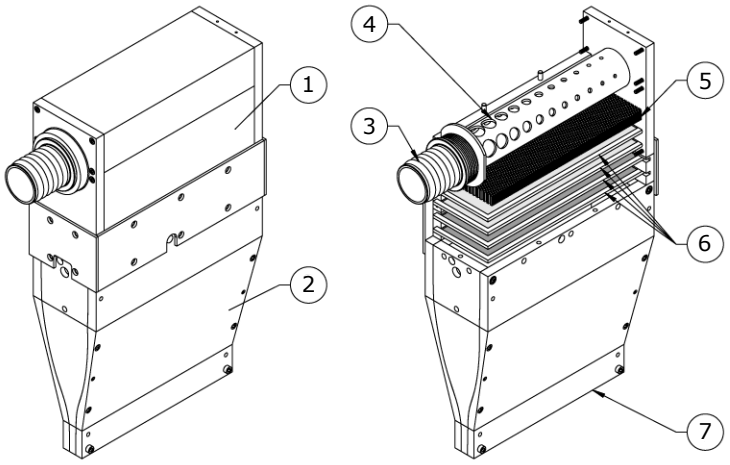

Figure 3.2: Jet nozzle assembly and flow conditioning elements. 1. Plenum and settling chamber 2. contraction and nozzle exit 3. inlet 4. flow distribution tube 5. honeycomb 6. steel mesh screens (light gray and dark gray indicates cell-to-diameter ratios of 0.68 and 0.7, respectively) 7. rectangular nozzle outlet. Figure adapted with permission from [57].

placed in the plenum. The cell length-to-diameter ratio of the honeycomb structure is 8.7. The four screens downstream of the honeycomb screen consisted of 2 pairs with open area ratios, of 0.68 and 0.7 respectively. The contraction section consists of a single block of machined aluminium and has a total length of $L_c = 0.25$ m. The contraction is achieved through two smoothly contoured, overlapping, cubic profiles and has an inlet to outlet area ratio of 9:1. The outlet section has a jet exit height (h) of 10 mm and span (w) of 200 mm which results in an aspect ratio (AR) of 20:1. The entire assembly was fixed in a horizontal position on an optical table as shown in Figure 3.1. The jet nozzle assembly was characterized in a previous study [57], where the flow along the centreline was found to be $95 \pm 0.5\%$ uniform in the spanwise direction. This calibration study was carried out at Re = 10,000 by calculating the velocity from measurements of dynamic pressure using a pitot-static tube. The measurements were recorded using a Setra Model 239 pressure

transducer connected to an NI PICe 6321 data acquisition board sampled at a frequency of 1000 Hz. The uncertainty is these measurements was quoted to 0.14% of full scale which corresponds to an uncertainty in velocity of ±2%.

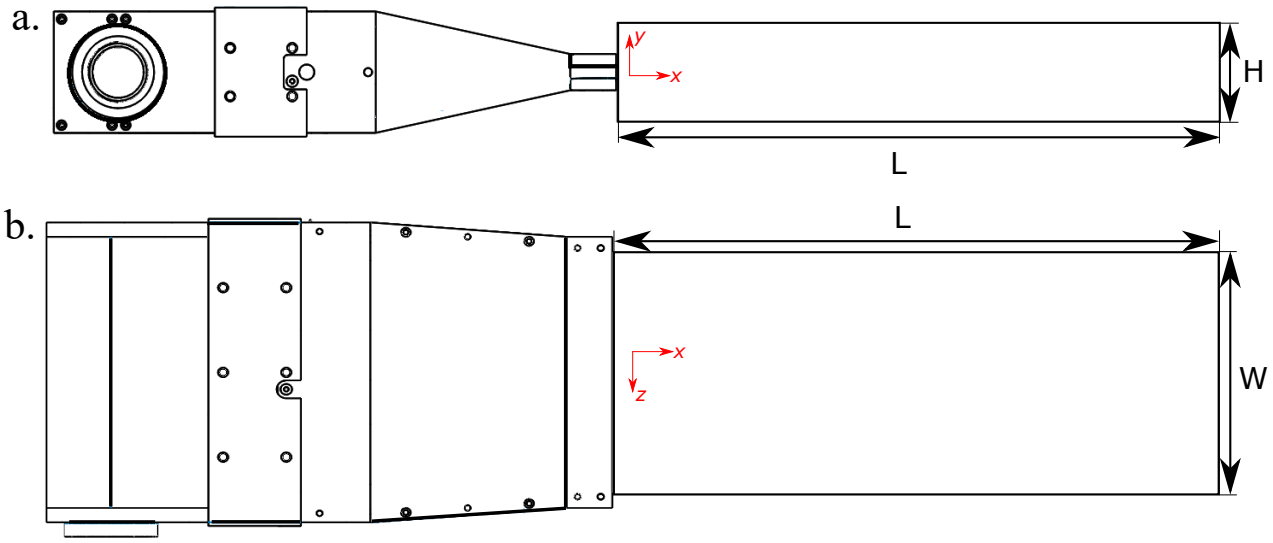

Figure 3.3: a. Side-view and b. Top-view of the confinement box placed at the jet exit. Coordinate system used throughout present study is shown

For the confined cases, two separate confined sections, corresponding to two different contraction ratios, were placed at the jet exit as shown in Figure 3.3. The confinement sections were manufactured from 6.35 mm thick plexiglass. The inner width (W) was matched to the jet exit span and was $20h$ wide. The confinement section stretched $50h$ (L) downstream of the exit. The two confinement ratios of 7 and 5 dictated the third dimension of the section (H) as $70h$ and $50h$ respectively. The confinement sections were adjusted in position using lab jacks whose bases were screwed into the optical table.

3.2 Particle Image Velocimetry

Time-resolved, PIV was used to capture the velocity field in unconfined and confined plane jet flows. A general overview of the method along with its theoretical background and operating principles may be found in the works by Westerwheel *et.al.* [14], Adrian and Westerwheel [58]. The overall arrangement of the system is shown in Figure 3.4. The Laser used for illumination was a Photonics DM20-257 Nd-YLF dual pulsed laser whose output was focused into a sheet of approximate width of 2 mm, using a LaVision unit consisting of spherical focusing lenses. The laser sheet was arranged so that the mid plane of the jet was illuminated. The main body of the laser was placed at a distance of greater than $70h$ downstream of the jet exit in order to avoid any adverse effects on the flow field. Flow seeding was accomplished using glycol-water particles with a mean diameter of approximately 1 μm.

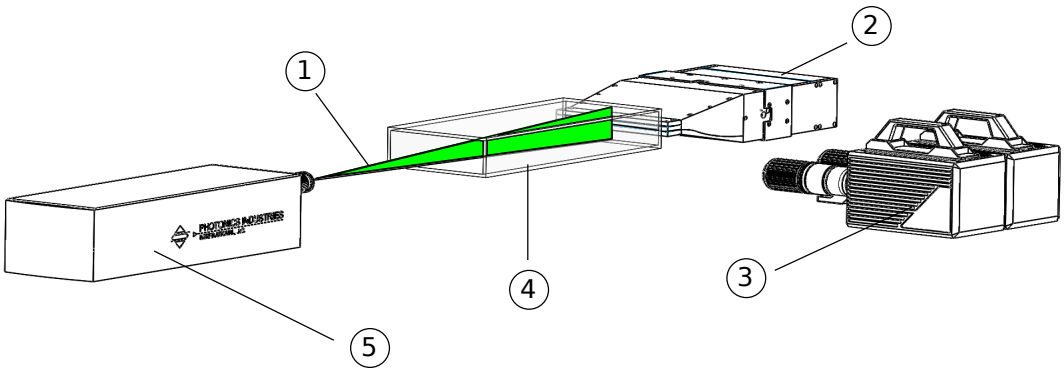

Figure 3.4: PIV arrangement : (1) Light Sheet, (2) Jet nozzle assembly, (3) Twin high speed cameras, (4) Transparent confinement box, (5) Laser.

Two Photron SA4 high speed cameras were used to image the flow field and were arranged as shown in Figure 3.4. Each camera had a sensor size of 1024 $\times$ 1024 px^2 and

the entirety of the sensor was used to image the flow field. Each camera was equipped with a 200 mm Nikon fixed focal length macro lens set at a numerical aperture of $f_{\#} = 8$. Flow field data were collected at four locations downstream of the jet exit as shown in Figure 3.5. Each Field of View (FOV) measured 3.2 h × 3.2 h with each downstream FOV overlapping with the corresponding upstream one over a distance of $0.9h$. The arrangements of the flow fields, their their extents relative to the jet exit and their overlaps are shown in Figure 3.5. Time resolved data were collected at fields of view numbered 1 and 2, over a single run. The camera arrangement was then moved downstream to collect time resolved data over fields of view 3 and 4. Each pair of velocity fields acquired from the images collected by the camera pair was then stitched together using cosine weighted function. The data was collected at a frequency of 1900 Hz (f_{ac}) in a dual-frame mode, with 2560 image pairs for each case. These parameters were identical for all three cases. The time-resolved data was used to study the vortex dynamics. In order to obtain the mean-fields, data was collected at a lower acquisition frequency of 125 Hz also in a dual frame mode with 2560 image pairs also obtained.

For the unconfined and two confined cases the cameras were calibrated using a calibration target with 0.02 mm grid spacing and common reference points in the overlap region. The calibration target was large enough so that both cameras could be calibrated at the same time without having to move the target. The alignment of the calibration target was achieved using a spirit level and the laser sheet. The average particle diameter that was imaged was 2-3 pixels (px).

The illumination and imaging hardware were synchronized by using a LaVision high speed controller which was also controlled by the aforementioned Davis 8.3 software. This software was also used to process the particle images. The particle images were pre-processed by applying a sliding minimum subtraction and intensity normalization in order

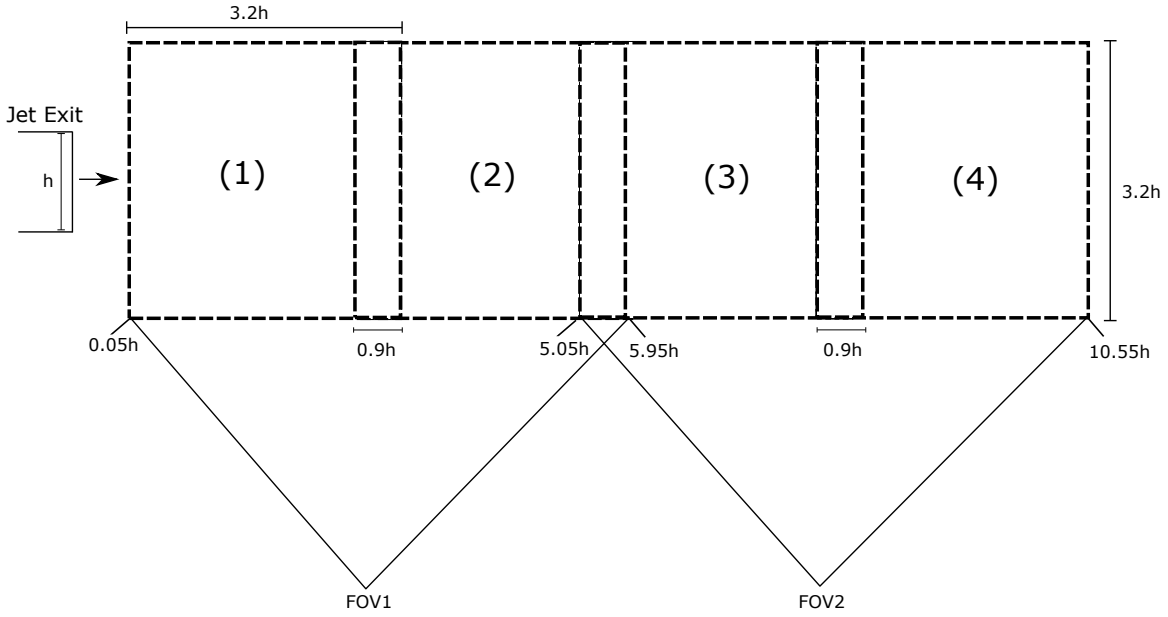

Figure 3.5: Extent of fields of view for PIV setup

to account for the difference in illumination in each frame. The images were then processed by applying a multi-pass, sequential cross- correlation algorithm with a decreasing window size. A final window size of 16 x 16 px^2 with 75% overlap was used. The final vector pitch obtained after processing was $0.019h$. The maximum uncertainty in the instantaneous velocity fields is estimated to be $\pm 8\%$ of U_0 with farther details of uncertainty analysis provided in Appendix A. A summary of the PIV parameters used is shown in Table 3.2.

In order to verify that the hydrodynamic frequencies of interest were not being forced by the blower settings, hot wire data was obtained at the centreline of the jet exit. The power spectral density of the fluctuations are plotted against the Strouhal number (St) in Figure 3.6. The range of frequencies which are linked to the shedding of coherent structures at the present Reynolds number (Re) are marked using dashed lines. The absence of peaks in the range shows that no forcing is occurring in this case.

Parameter	Value	Unit
Laser	Photonics DM20-527 Nd-YLF	–
Camera(s)	2 x Photron SA4	–
Lens focal length	120	mm
$f_\#$	8	–
Sensor size	1024 x 1024	px^2
Magnification	0.625	–
Sample Rate (Time-Resolved)	1.9	KHz
Sample Rate (Mean)	125	Hz
Final window size	16 x 16	px^2
Vector Pitch	$0.019h$	–

Table 3.1: PIV experimental parameters

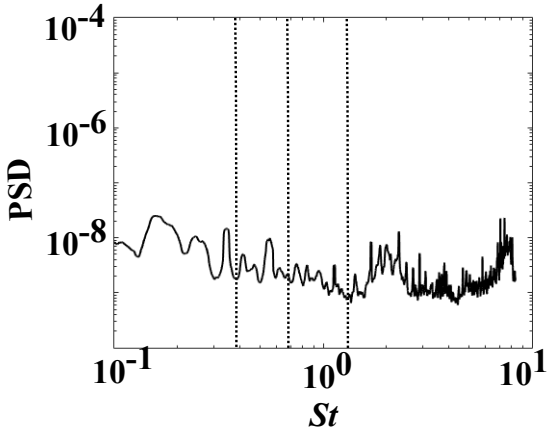

Figure 3.6: Power Spectral Density of fluctuations from hot wire data, with markings showing the hydrodynamic frequency of interest, its subharmonic, and its higher harmonic.

Chapter 4

Results and Discussion

This chapter presents the results obtained from performing the experiments described earlier and provides accompanying discussions. The effects of confinement on the mean and turbulent flow characteristics of the planar jet are initially examined. Building on the understanding of these time-average quantities, the development and evolution of coherent structures are then investigated. Finally, Proper Orthogonal Decomposition (POD) analysis is performed in order to obtain quantitative estimates of the most energetic structures in the flow.

4.1 Time Averaged Statistics

The changes in mean velocity fields due to confinement are explored through the use of iso-contour maps of mean velocity (U) in Figure 4.1. The data have been normalised by the centreline velocity (U_0) at a streamwise location of $0.05h$, corresponding to the most upstream location in the fields of view (FOV). The contour maps show the presence of a

distinct core of high streamwise velocity, surrounded by lower velocity entrained co-flow, for all three cases. This results in the profiles of mean streamwise velocity at the jet exit having a so called 'top-hat' shape characteristic of plane jets (Figure 4.2). The presence of a small entrained co-flow in the unconfined case is speculated to be due to global recirculation within the experimental facility. The velocity of the co-flow at a streamwise location of $0.05h$ in the unconfined case is $0.05U_0$ while, for the confined cases, the values are greater than the unconfined case at $0.28U_0$ for CR = 7 and $0.34U_0$ for CR = 5.

The quantitative comparison of the decay in the centreline velocity between the confined and unconfined cases is shown in Figure 4.3. Downstream of the jet exit, the centreline velocity in the unconfined case shows an increase to $1.02U_0$ at $x/h = 4$ and thereafter decays downstream. The data in the decay region are in good agreement with hot-wire data obtained from a planar jet flow with a jet exit Reynolds number (Re) of 4000 by Deo *et. al.* [25]. For the confined cases centreline flow also accelerates downstream of the jet exit reaching a maximum value of $1.05U_0$. The centreline velocity then decays at a rate slower than the unconfined case. This may be an indication of the formation of a recirculatory bubble at the confinement walls, downstream of $x/h = 10$, as has been observed in studies of high Reynolds numbers axisymmetric jets [1, 2].

The differences in the jet spreading in the streamnormal direction, between unconfined and confined cases are quantified by the growth of the jet half-width downstream as shown in Figure 4.4. The jet half-width ($y_{0.5}$) is defined as the distance, in the streamnormal direction, from the jet centreline to the location where the velocity drops to half of the local centreline velocity. The spread rate of the confined cases is lower than that of the unconfined cases. The unconfined case shows a non-dimensional half-width spread rate of 0.06, which compares well with the study of a plane unconfined jet by Thomas and Chu (Re = 5000) [36]. The corresponding values for the two confined cases, within experimental

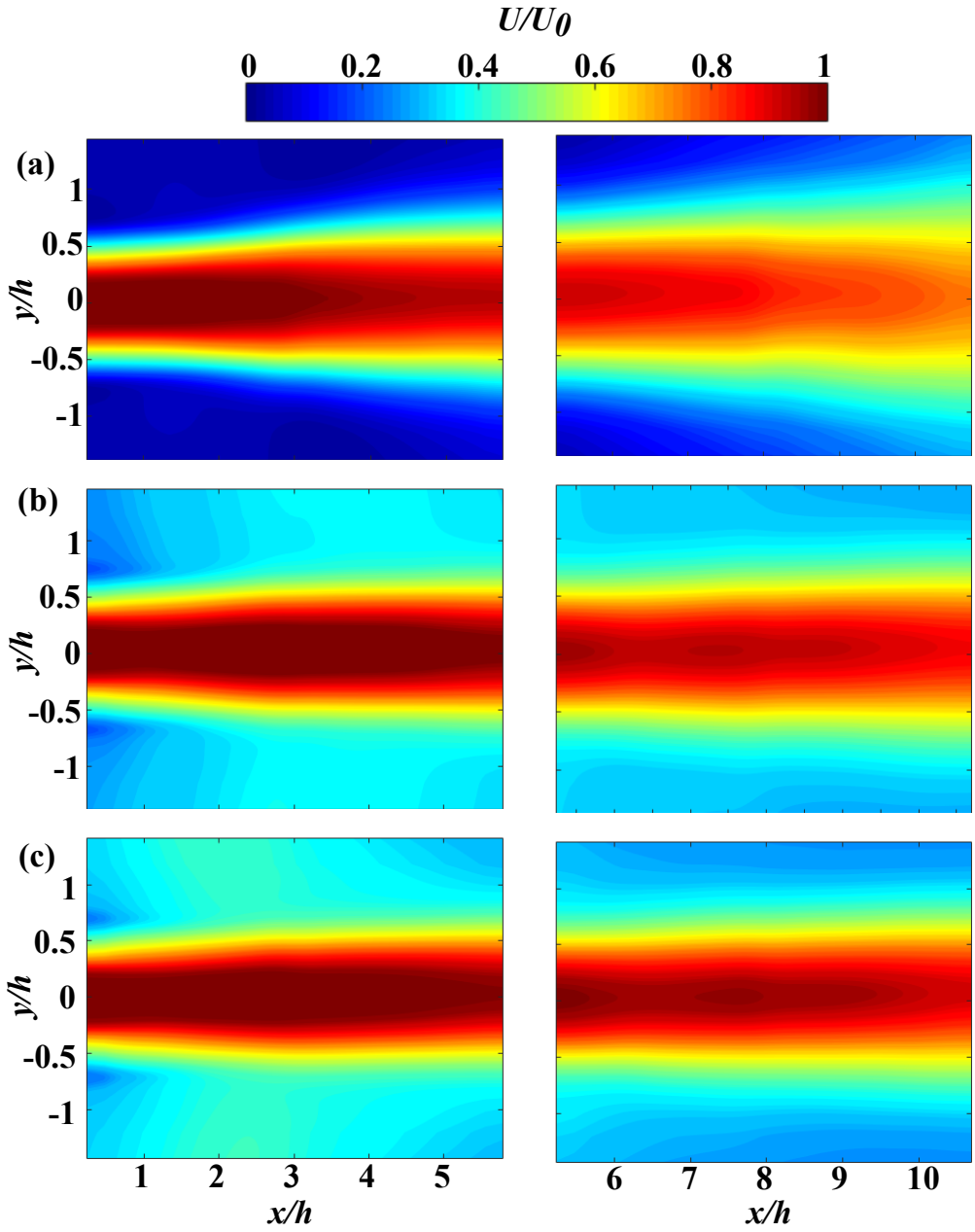

Figure 4.1: Contours of time-averaged velocity normalised by mean exit velocity of the jet (U_0) for (a) Unconfined, (b) CR = 7, and (c) CR = 5.

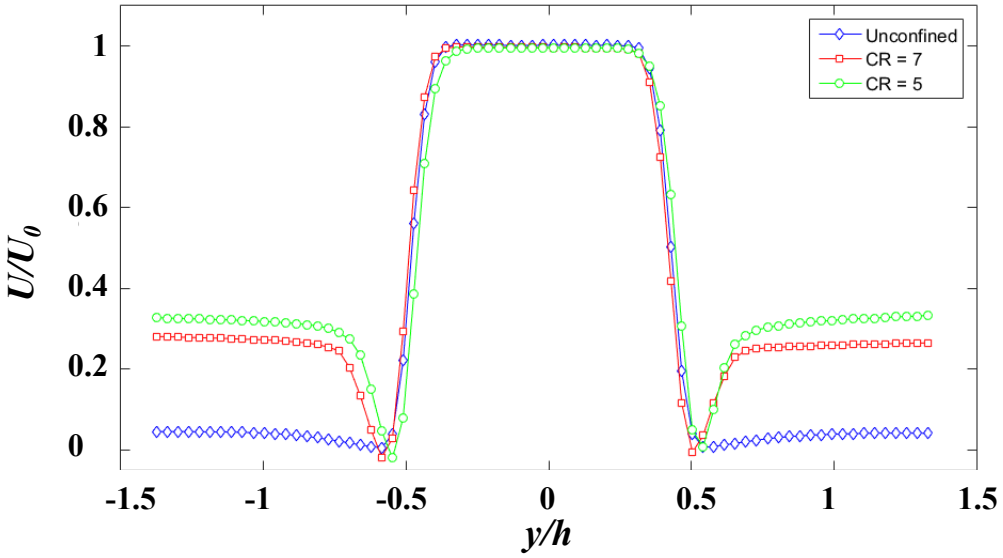

Figure 4.2: Normalised velocity profiles at $x/h = 0.05$.

uncertainty, is 0.03. The spread rate of the jet quantifies the rate of diffusion of momentum from the high velocity jet flow to the surroundings. The lower growth rate of the confined cases indicates that a larger proportion of the core jet momentum is preserved as the flow travels downstream. The higher co-flow in these cases results in a lower velocity gradient between the co-flow and the main jet flow resulting in lower momentum diffusion from the main jet flow into the surrounding co-flow.

Previous studies in the self-similar region of confined axisymmetric jets [1, 2, 50], and of unconfined jets with variable co-flows [16, 15], observed that an increase in co-flow led to a decrease in the decay rate of the centreline velocity and spread rate of the jet. Although the self-similar region for the plane confined jet cases has not been measured in the present study, the trends obtained, are aligned with the general conclusions in literature.

The effect of the confinement on turbulence statistics is examined next. Figures 4.5, 4.6 and 4.7 show the contour plots of the normalised values of root-mean-square of streamwise

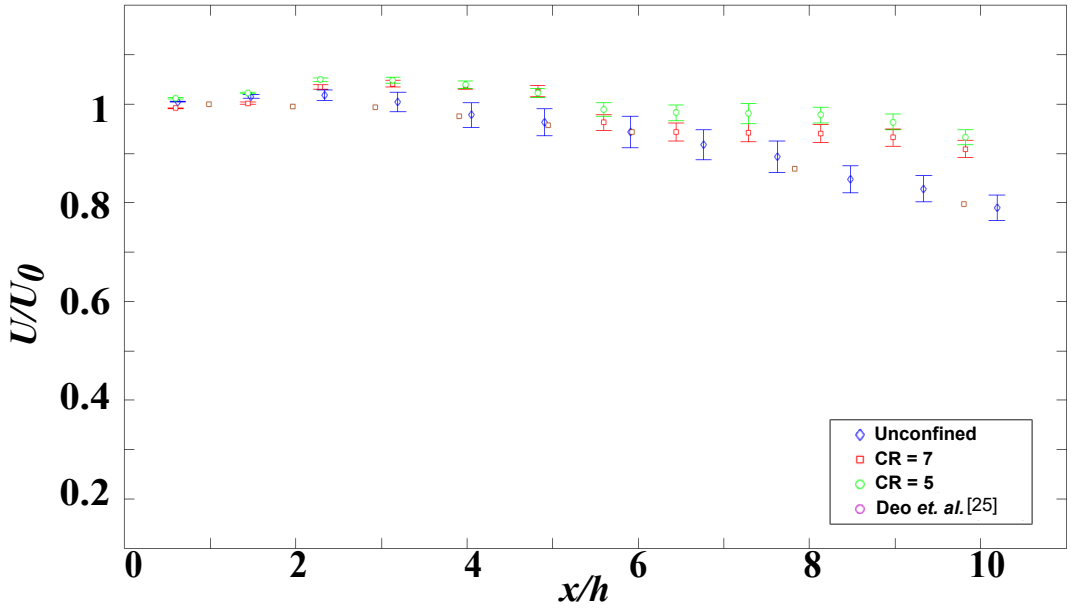

Figure 4.3: Mean centreline velocity variation. Data from Deo *et al.* [25] (Re = 4000) are included for comparison.

fluctuations (u_{rms}), root-mean-square of stream normal fluctuations (v_{rms}) and Reynolds Shear Stress *(RSS)*. The figures show the two separate FOVs. The figures have not been stitched since the data were collected over separate experimental runs and therefore are uncorrelated in time. The variation of these quantities along the shear layer is shown in each case as an inset plot attached to each figure. The contour plots show that the maximum values of u_{rms}/U_0 are present along the centreline while for v_{rms}/U_0 the highest values lie along the shear layer. The values of u_{rms}/U_0 and v_{rms}/U_0 along the shear layer, for the unconfined case, compare well to the work of Thomas and Goldschmit [32] (plane unconfined jet, Re = 6000). Notably, for both variables, the values along the shear layer for the confined cases are lower than those of the corresponding unconfined case, with the CR = 7 case having slightly greater level of velocity fluctuations than the CR = 5 case by an average of 15% over the observed domain. The region of high streamwise turbulent

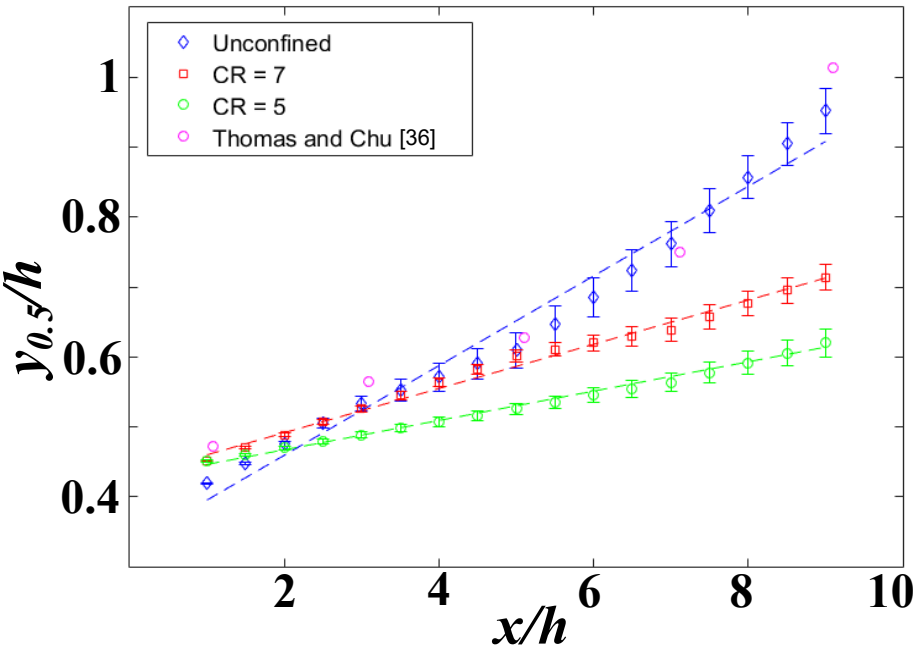

Figure 4.4: Variation of jet-half width. Linear fits to data are shown by dashed lines. Data from Thomas and Chu [36] (Re = 5000) are included for comparison.

fluctuations (u_{rms}/U_0) arises as the shear layers on either side of the jet centreline meet at the end of the potential core (Figure 4.1). The contour plots in Figure 4.5 indicate that, for the confined cases, the shear layers meet farther downstream as compared to the unconfined case. This is due to the lower spread rate of the jet in the confined cases, as has been discussed previously (Figure 4.4). The streamnormal fluctuations (v_{rms}/U_0) are concentrated in the shear layers for all three cases. These energetic fluctuations are due to the dynamics of coherent structures that form in the shear layer which are discussed in the following sections.

The contour plots in Figure 4.7 show that the highest magnitudes of RSS are concentrated in the shear layers for all three cases. The regions of high RSS values are seen to widen downstream as the jet spreads, with the unconfined case showing the largest increase

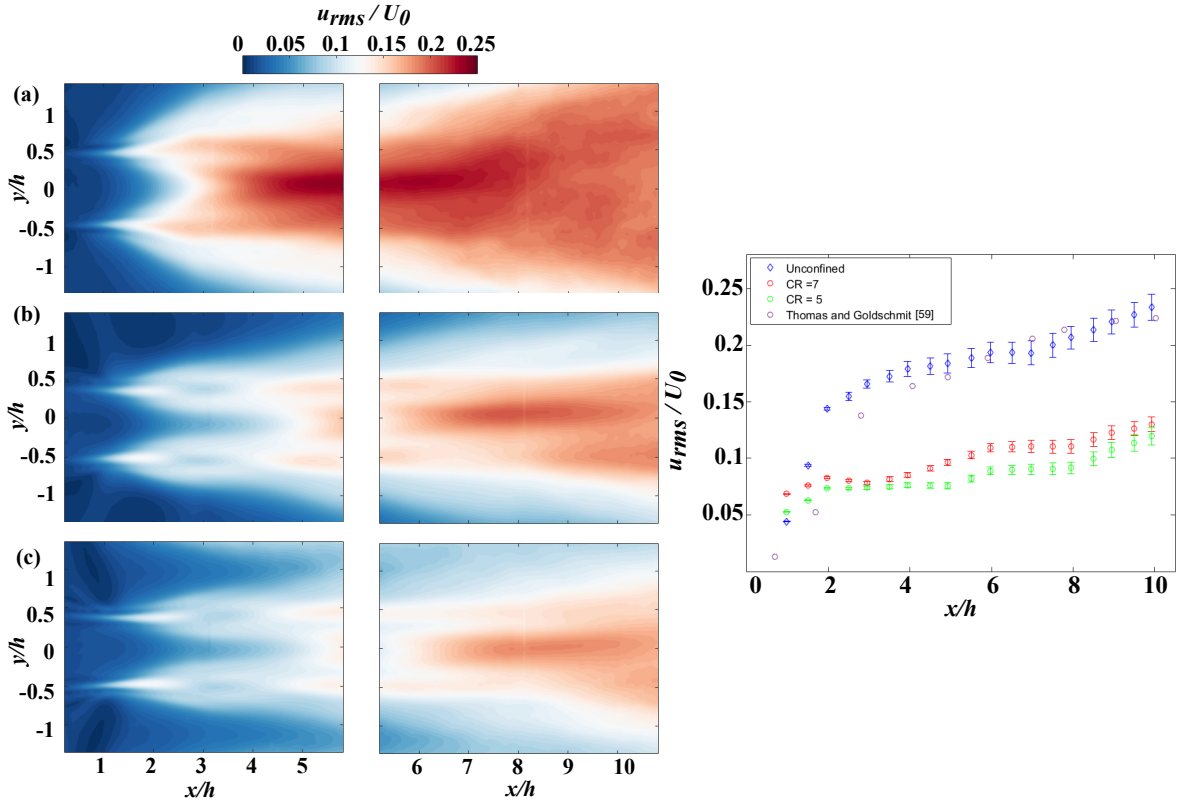

Figure 4.5: Contours of normalised u_{rms} for (left) (a) Unconfined, (b) CR = 7 and (c) CR = 5. The inset (right) shows u_{rms} variation along the shear layer including data from Thomas and Goldschmit [59] (Re = 6000)

in RSS. For the unconfined case, the values of RSS increase from a distance of $x/h = 4$ downstream of the jet exit, and are seen to plateau downstream of $x/h = 8$. The data show good agreement with that of Browne et. al. [60]. However, both the confined cases notably smaller RSS values with lower rates of growth.. The confined jet flows experience a lower shear due to the higher co-flow which, in turn, is responsible for the lower values of RSS observed in the shear layer.

Therefore, the RMS of turbulent fluctuations and the RSS in the shear layer are seen to be the largest in the unconfined case and decreases with increasing confinement ratio.

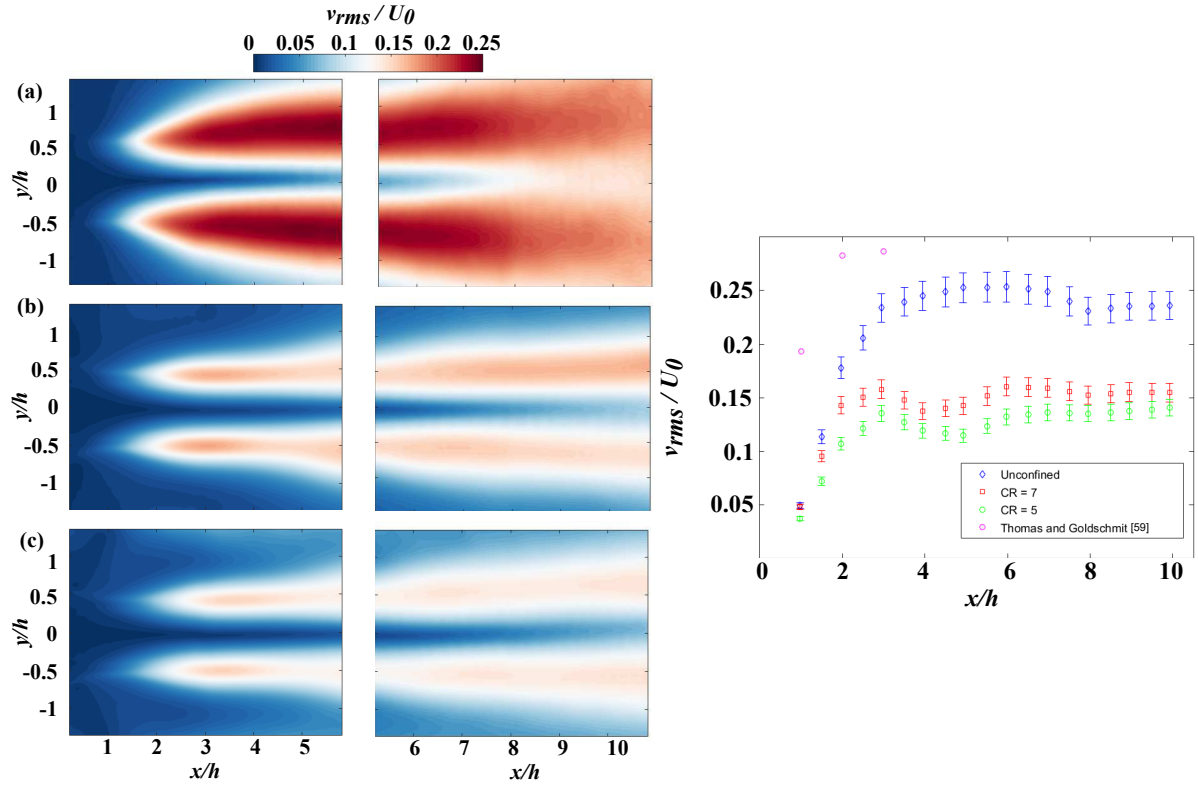

Figure 4.6: Contours of normalised v_{rms} (left) for (a) Unconfined, (b) CR = 7 and (c) CR = 5. The inset (right) shows v_{rms} variation along the shear layer including data from Thomas and Goldschmit [59] (Re = 6000)

The lower values of shear stress in the confined cases leads to less mixing, and lower diffusion of momentum from the main jet flow to the co-flow. This explains the lower jet spread rate observed in the confined cases in the previous section. These observations are also consistent with previous studies involving axisymmetric jets with variable co-flows in confined [15] and unconfined [16] jets, which observed that an increase in co-flow decreased the RSS in the shear layer. These studies were conducted at Reynolds numbers in the range 52000−295000 and, therefore, are not directly comparable with the present experiments. However, they support the overall observed trends of decreasing magnitudes of turbulence statistics with increased co-flow.

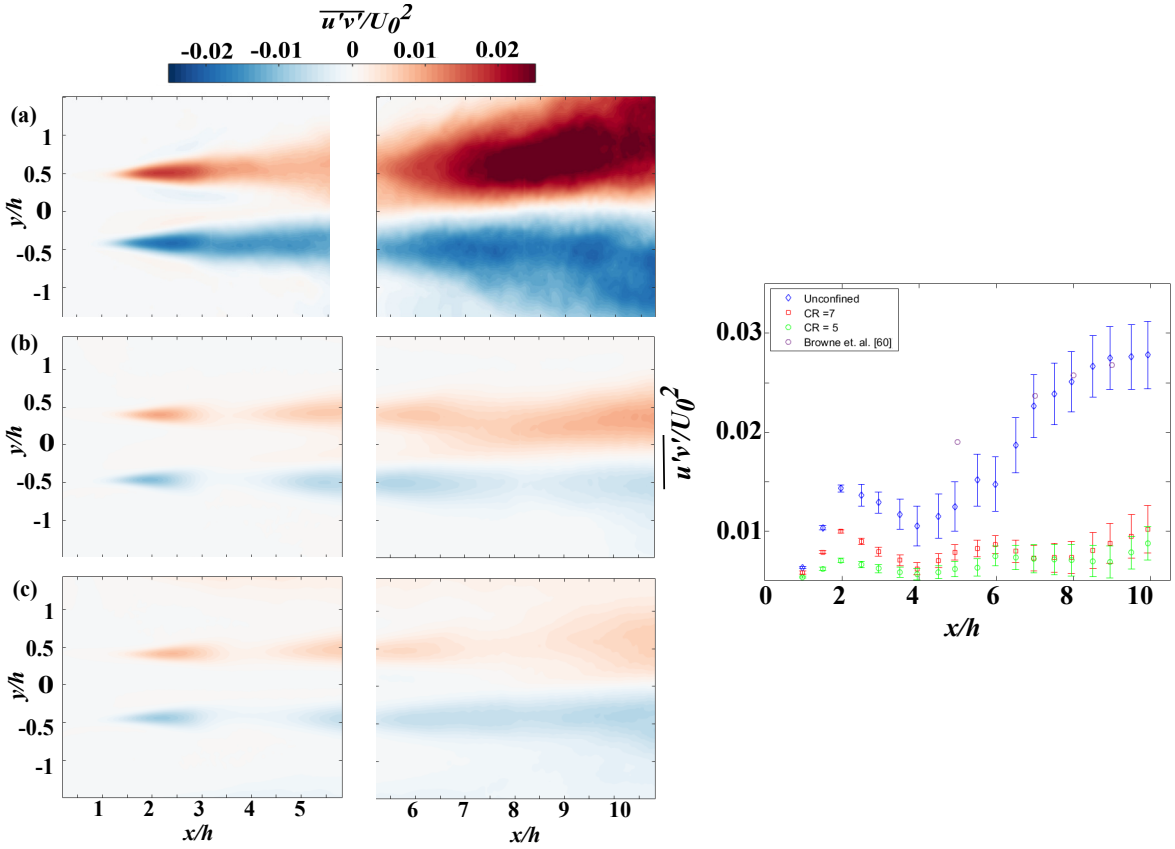

Figure 4.7: Contours of normalised Reynolds Shear Stress (left) for (a) Unconfined, (b) CR = 7 and (c) CR = 5. The inset (right) shows RSS variation along shear layer (right) including data from Browne *et. al.* [60] (Re = 6000).

4.2 Dynamics of Coherent Structures

It was shown in Chapter 2 that the shear layers of planar jet flows are unstable due to the Kelvin-Helmholtz instability. Therefore, velocity fluctuations in the shear layers are amplified until the shear layers roll up to form coherent structures. As has been noted in the previous section, confinement results in changes to the mean turbulence statistics in the shear layers of the planar jet flow. In this section, the corresponding changes in the coherent structures due to the confinement are investigated.

The spatio-temporal development of coherent structures is vizualised by a series of vorticity contour snapshots in Figures 4.8 and 4.9. Each frame is separated by a non-dimensional time of $5U_0/(f_{ac}h)$. The vorticity (ω_c) is calculated using the 8-point line integral method [61]. In order to further assist in coherent structure identification, the contours of λ_2 criterion proposed by Jeong and Hussain [62] are also plotted in Figures 4.8 and 4.9.

The coherent structure development for the unconfined case is shown in Figure 4.8. The upstream FOV shows the formation and shedding of Vortex A1 in the shear layer. The vortex is formed and shed over two frames which corresponds to a normalised time of 1.5 and the normalised shedding frequency ($St_0 = fh/U_0$) of the primary structures is therefore estimated to be $St_0 = 0.7$. After shedding, the vortex S1 is convected downstream along the shear layer and undergoes pairing with vortex S2 to form D1. Structure D2 is also seen to form as a result of pairing of two primary vortices, upstream of D1. Thus, for the unconfined case, the primary vortices are seen to undergo pairings over a streamwise distance of between $x/h = 2.5$ and $x/h = 4$ downstream of the jet exit. Nearly all structures shed from the shear layer were observed to pair in 2560 time-resolved snapshots of the flow field. As the structures pair, the characteristic streamwise wavelength (λ_{x0}) doubles, as has been noted by previous studies [41, 44]. In the frames covering the downstream FOV for the unconfined case, the most striking feature observed, is the loss of coherence of the structures.

The coherent structures for the CR = 7 case are shown in Figure 4.9. Structure S2, which is a primary vortex, completes the shedding process over two frames thus leading to a shedding frequency of $St_0 = 0.7$ that is similar to the unconfined case. Furthermore, S1 and another primary vortex S2 do not undergo pairing over the first FOV. The pairing of primary tructures, which leads to the doubling of the separation wavelength from the

initial λ_{x0} to $2\lambda_{x0}$, takes place in the frames covering the downstream FOV. Of interest is the emergence of structures separated by wavelengths of $2.5\lambda_{x0}$. The process of the formation of these structures is detailed in a sketch shown in Fig 4.10. These structures are formed when a single unpaired structure and a paired structure merge forming what is termed as a "triplet". The structures in the CR = 5 case show qualitative behavior that is very similar to the CR = 7 case and hence the corresponding vorticity sequences are not presented here for brevity.

The differences in the development of the coherent structures account for the differing rates of jet spread observed earlier. The growth of the shear layers, and thus the spread of the jet, is driven by the successive pairings of the coherent structures [63]. As the structures pair up, the shear layer thickens and the jet spreads. Therefore, as the pairings are delayed over an equivalent streamwise distance for the confined cases, their jet spread rate is also lowered.

Figure 4.11 shows the plots of Power Spectral Density (PSD) of streamnormal velocity fluctuations ($v^{'}$). The spectra are obtained by sampling locations in the shear layer at successive streamwise locations for the unconfined and confined cases. The PSD are plotted against the Strouhal number $St = fh/U_0$. For the unconfined case, at a distance of $x/h = 0.5$ downstream of the jet exit, the spectra show the amplification of a band of frequencies between $St = 0.6$ and $St = 0.75$ with a peak observed at $St_0 = 0.67$ for the spectrum at $x/h = 0.5$. This frequency corresponds to the passage of vortices formed from the initial roll up of the shear layer and falls within the range of passage frequencies ($0.35 \leq St_0 \leq 0.75$) of primary vortices established by previous experiments involving plane free jets [24, 28, 64]. Further downstream, the spectra at successive sampling locations show that this band of amplified frequencies broadens and progressively shifts towards lower frequencies. The broadband peak observed is a characteristic of developing shear flows and

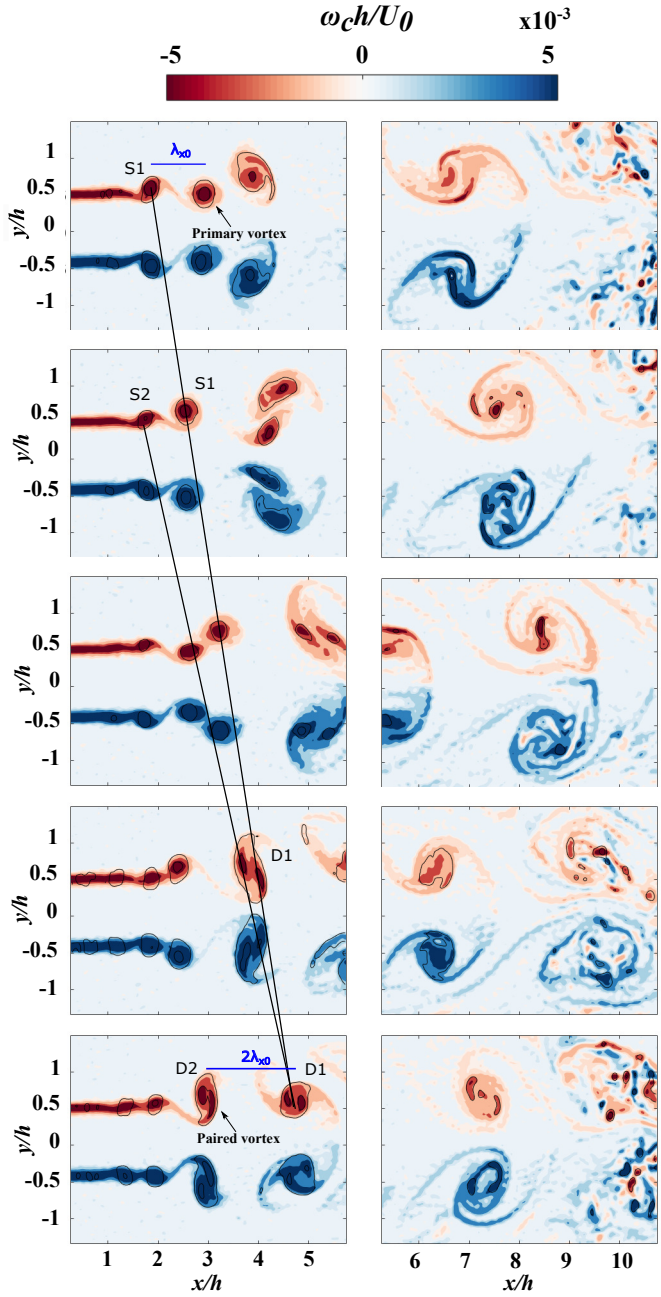

Figure 4.8: Contours of normalised vorticity and λ_2 criterion showing the passage of coherent structures for the unconfined case in both FOVs.

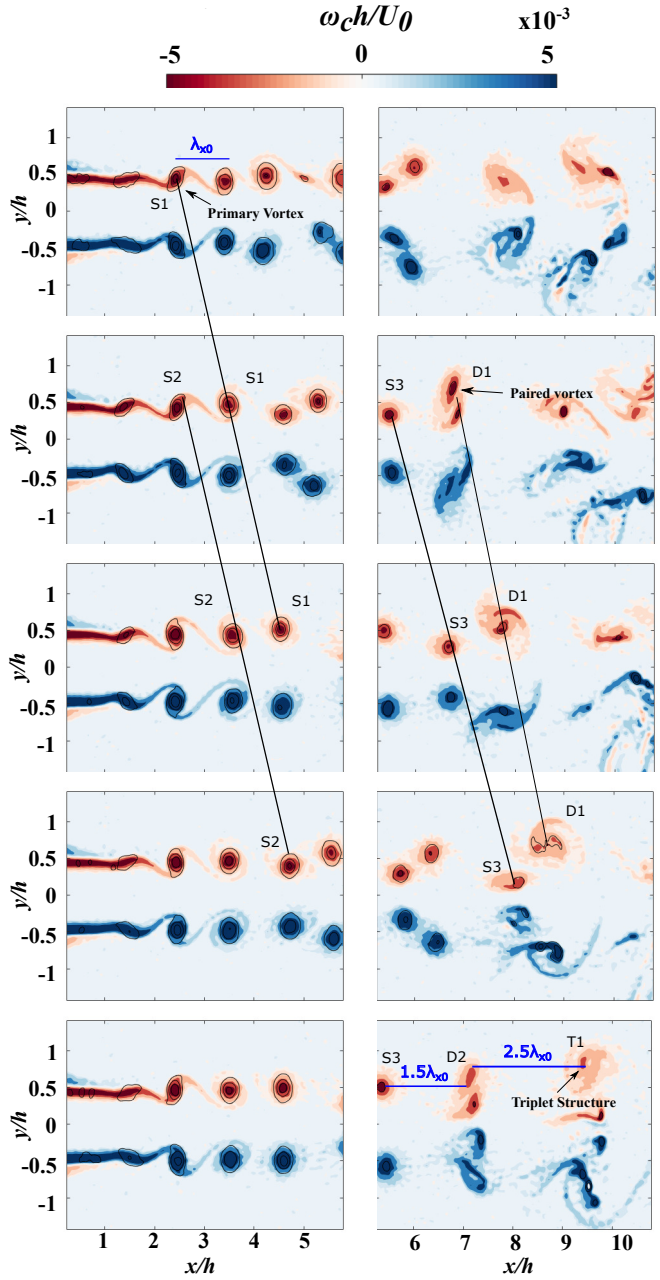

Figure 4.9: Contours of vorticity and λ_2 criterion showing coherent structures for the CR = 7 case in both FOVs.

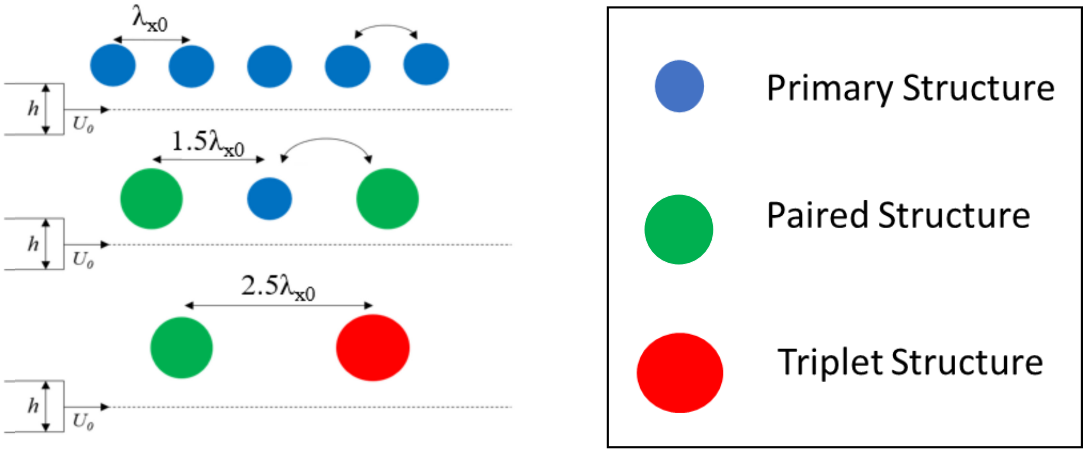

Figure 4.10: Sketch showing the formation of the "triplet" structure present in the confined cases.

the shift of the peak towards lower frequencies is due to successive merging and pairing of structures, [43] which has been discussed in the previous section.

The confined cases, both CR = 7 and CR = 5, show similar spectral characteristics. A peak with high energy content at $St_0 = 0.67$, is observed for both cases at $x/h = 0.5$. The spectra remains relatively unchanged at successive sampling locations in the shear layer till a distance of $x/h = 5$ downstream of the jet exit. Farther downstream, the spectra for the confined cases shows a broader peak of amplified frequencies roughly centred around $0.4St_0$. This frequency corresponds to the "triplet" pairing events, an example of which was outlined in the earlier section. This indicates that the successive pairings that lead the spectral peak of the unconfined case to broaden and shift to lower Strouhal numbers, take place farther downstream for the confined cases as compared to the unconfined case.

Figure 4.12 shows the contour plots of the wavenumber-frequency spectrum of stream-normal fluctuations $v^{'}$ plotted for both FOVs and all three cases. The two-dimensional

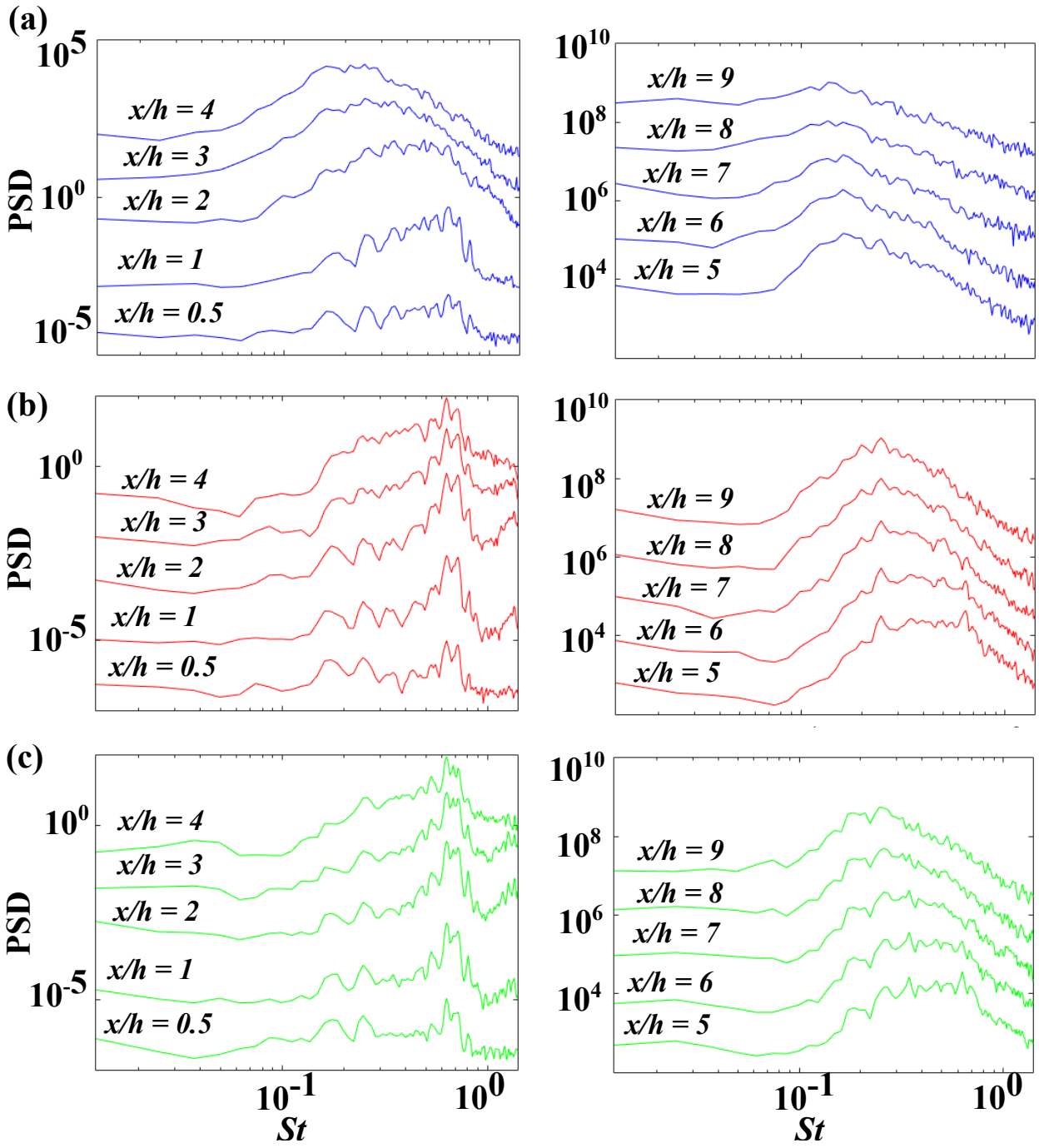

Figure 4.11: PSDs of $v^{'}$ along shear layer. Each spectrum has been stepped by an order of magnitude for clarity. (a) Unconfined, (b) CR = 7, and (c) CR = 5.

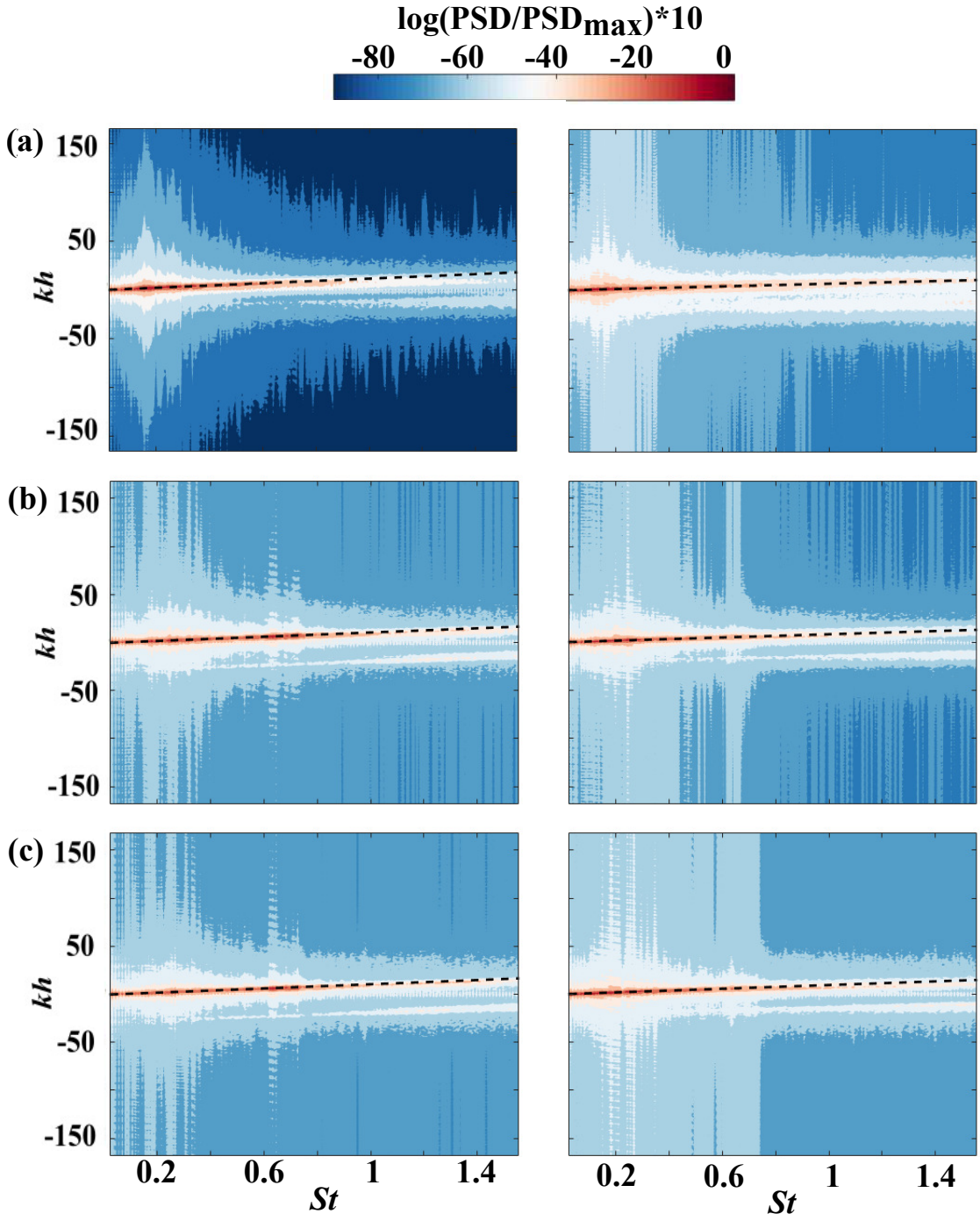

Figure 4.12: Frequency-wavenumber spectra. (a) Unconfined, (b) CR = 7, and (c) CR = 5. The dashed black line is a linear fit to the locations of maximum spectral energy.

spectra are computed from fluctuations at points extracted along the shear layer, based on the locations of maximum RSS. The spatial and temporal dimensions of the input data were 312 and 2560 points respectively. This results in a frequency resolution of $\Delta St = 0.06$ and a wavenumber resolution of $\Delta kh = 1.11$. The primary feature observed in all the spectral plots is the linear trend of the maximum energy across the entire range of frequencies. This is known as a convective ridge [65] and is a feature of physical phesymena which have convective periodic fluctuations, e.g. travelling waves [66, 67]. The convective ridges for the different cases are highlighted in Figure 4.12 by solid black lines. These lines are a linear fit to the points of maximum spectral energy and their slope provides an estimate of the group velocity of wave packets [65], or the convective velocity of the coherent structures in this case. It should be noted that in all sub-plots of Figure 4.12 a secondary ridge-like structure at negative wavenumbers may be observed. This is a result of aliasing and does not reflect the true convective velocity. The convective velocity for the structures is obtained from the relation $U_{cv} = 2\pi f/k$ where f and k are the frequency and wavenumber obtained from the linear fit. Table 4.2 shows the convective velocities of the coherent structures in all three cases. These are reported in terms of U_0 and for the unconfined case the values correspond to $0.57U_0$ in FOV1 and $0.56U_0$ in FOV2. These values increase to $0.64U_0$ in FOV1 and $0.62U_0$ in FOV2 for the confined cases. For each case the mean convective velocity of the structures is seen to be lower in the downstream FOV. Additionally, the average convective velocity of the structures is observed to be higher in the confined cases. This increase may be explained in terms of the stronger co-flow experienced by the confined cases as shown in the contour plots of the mean velocity data. This leads to a larger average velocity experienced by the structures in the shear layer in the confined cases and leads to the trends observed in Table 4.2.

The wavenumber-frequency spectra also provide estimates of the wavelengths associated

Case	FOV1	FOV2
Unconfined	$0.57U_0$	$0.56U_0$
CR = 7	$0.64U_0$	$0.62U_0$
CR = 5	$0.64U_0$	$0.62U_0$

Table 4.1: Convective velocity estimates from wavenumber-frequency spectra.

Case	St_0	$St_0/2$	0.4 St_0
Unconfined	$0.8h$	$1.7h$	–
CR = 7	$1.1h$	$2h$	$2.5h$
CR = 5	$1.1h$	$2h$	$2.5h$

Table 4.2: Streamwise wavelength estimates at shedding frequencies, their subharmonic, and "triplet" structures from wavenumber-frequency spectra.

with the coherent structures. These are obtained from the relation $\lambda_x = 2\pi/k$ where k is the wavenumber corresponding to the frequency of interest obtained from the wavenumber frequency plots and are shown in Table 4.2. For the unconfined case, the wavelength corresponding to the frequency representing the passage frequency of the initial structures (λ_{x0}) is estimated as $0.8h$. The wavelength corresponding to $St_0/2$ is estimated to be $1.7h$ which is, as expected, roughly twice that λ_{x0}. For the confined cases, the estimate of the primary wavelength corresponding to St_0 is longer than the unconfined case at $1.1h$. The wavelength estimates for the first subharmonic and the "triplet" pairing frequency for both confined cases show the expected trends of increasing by 2 and 2.5 times, respectively.

Figures 4.13 and 4.14 show the spatial distribution of the normalised root-mean-square of band-pass frequency filtered streamnormal velocity fluctuations ($< \hat{v} > /U_0$), filtered at the primary passage frequency, ($St_0 \pm 0.05$) and its first subharmonic ($St_0/2 \pm 0.05$). The peak of these fluctuations is observed to be at a point further upstream for the unconfined case than the confined cases, while the magnitude of the peak fluctuation also decreases for

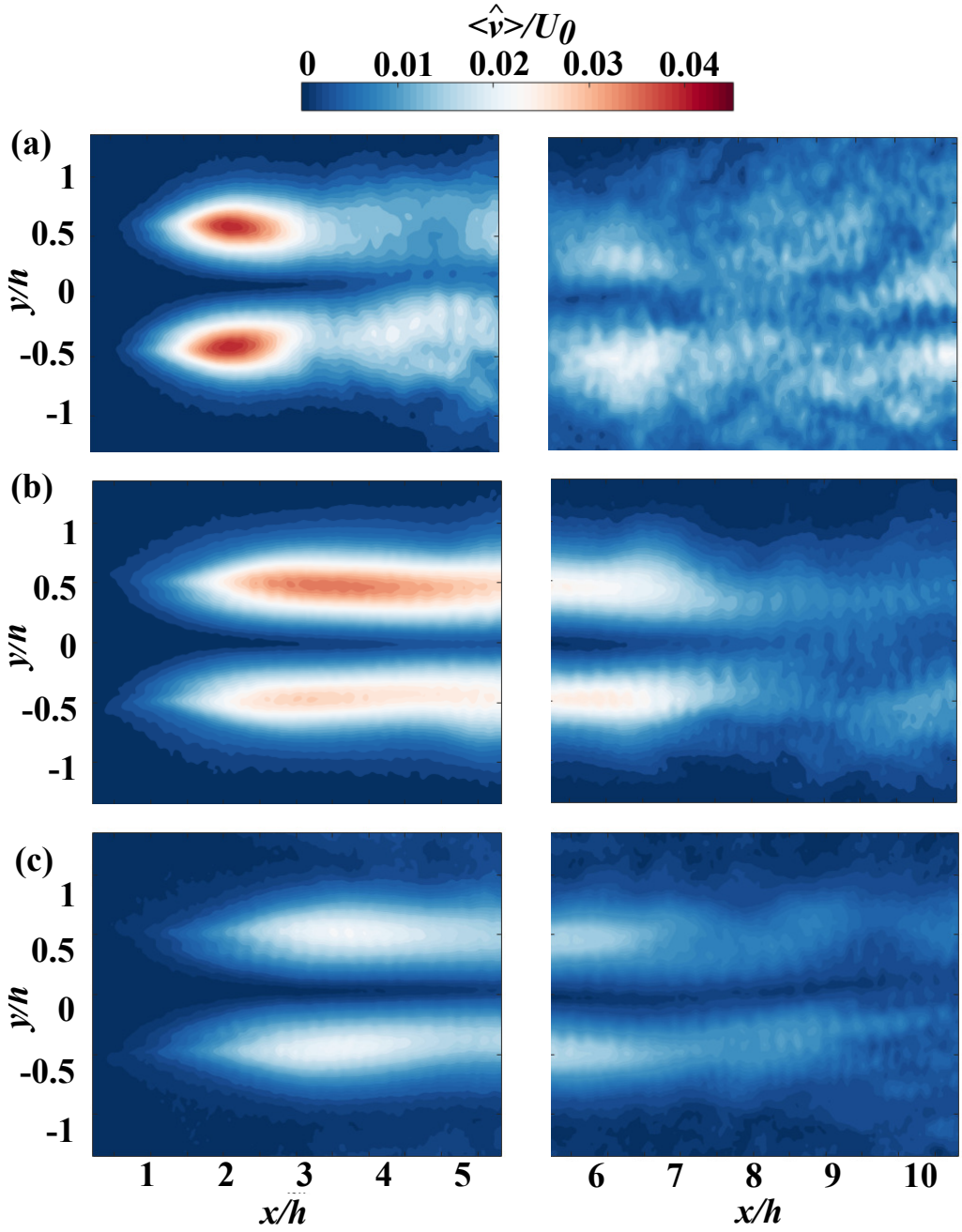

Figure 4.13: Contours of root-mean-square of band-pass filtered vertical velocity fluctuations $< \hat{v} >$ filtered at $St_0 = 0.67 \pm 0.05$ for (a) Unconfined, (b) CR = 7, and (c) CR = 5.

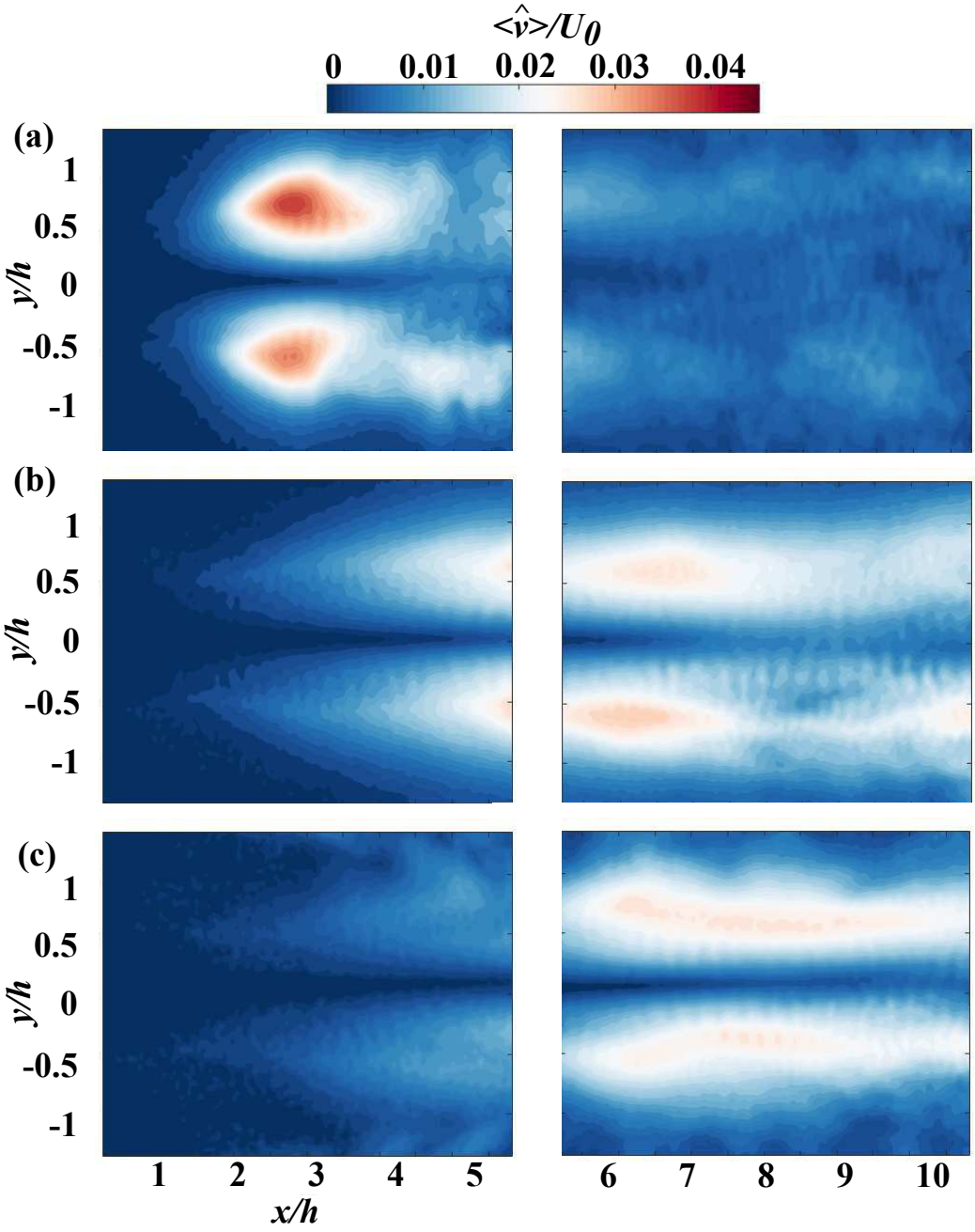

Figure 4.14: Contours of root-mean-square of band-pass filtered vertical velocity fluctuations $< \hat{v} >$ filtered at $St_0/2 = 0.34 \pm 0.05$ for (a) Unconfined, (b) CR = 7, and (c) CR = 5.

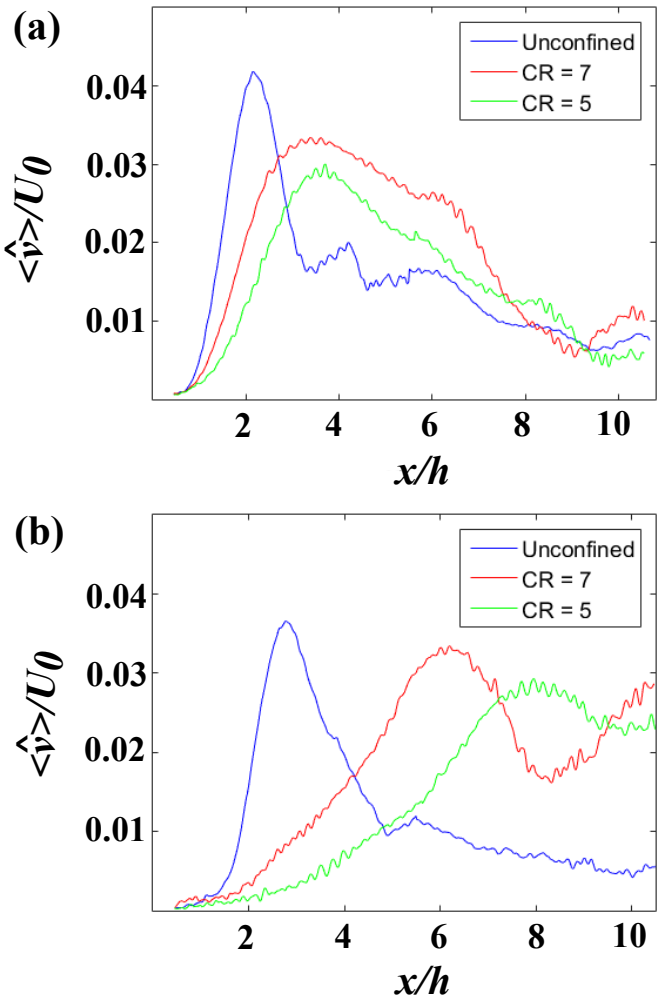

Figure 4.15: Plots of frequency band-pass fluctuations along shear layer for (a) $St_0 = 0.67 \pm 0.05$ and (b) $St_0/2 = 0.34 \pm 0.05$.

the confined cases as compared to the unconfined case. Figure 4.15 shows the corresponding line plots obtained by extracting $< \hat{v} >$ along the points of maximum RSS in the shear layer. The frequency filtered fluctuations are seen to grow exponentially, downstream of the jet exit, and their values reach a peak before decaying further downstream. For the unconfined case, the fluctuations filtered at St_0, shown in 4.15(a), peak at $x/h = 1.8$, while in the confined cases the rate of growth of fluctuations is lower and corresponding peak locations are farther downstream at $x/h = 3.1$ and $x/h = 3.7$ for the CR = 7 and CR = 5 cases, respectively. The fluctuations in the shear layer grow due to the instability in the shear layer as been mentioned earlier. The location of the peaks of the fluctuations filtered at St_0 roughly indicate the location of the roll up of the shear layer and the formation of primary structures. The locations of these peaks also correspond to the onset of growth of the fluctuations filtered at the subharmonic $St_0/2$, as shown in Figure 4.15(b). The peak value of the fluctuations filtered at the subharmonic for the confined cases is attained downstream of that for the unconfined case. As the subharmonic is associated with the structures formed from the pairing of two primary vortices, this indicates that, for the confined cases, the location of pairing is also shifted farther downstream as compared to the unconfined case. Additionally, the growth rates of the fluctuations filtered at the subharmonic are lower for the confined cases as compared to the unconfined case.

4.3 Proper Orthogonal Decomposition

Proper Orthogonal Decomposition (POD) is a modal decomposition technique that extracts modes based on optimizing the mean square values obtained from experimentally or numerically derived flow fields [68]. It was first introduced into the fluid mechanics community by Lumley [69]. The technique decomposes a set of flow field data into a series of basis functions ranked in order of energy. In the present study, POD analysis is carried out on the velocity fields using the method of snapshots [70]. This method first constructs a matrix composed of the time-series of snapshots of the fluctuating velocity fields namely, $u'^T u'$ and $v'^T v'$, where the superscript T indicates the transpose of a matrix. The corresponding eigenvalues (λ_i) and spatial modes ($\vec{\psi_i}$) are obtained by solving the eigenvalue problem for this matrix. The eigenvalue λ_i represents the turbulent kinetic energy present in the i^{th} mode. The method of snapshots also yields the temporal coefficients (a_i), which can be used to reconstruct the fluctuating velocity field in every mode by the relation $\vec{u'} = \Sigma_{i=1}^{N} a_i \vec{\psi_i}$. This section presents the results of POD analysis on 2560 velocity snapshots, for each case, obtained from PIV at a frequency of 1.9 KHz for both unconfined and confined cases.

The relative energies of the twenty most energetic spatial modes for all three cases and over two FOVs are shown in Figure 4.16. The first eight most energetic modes appear as four mode pairs for all cases. This is indicated by their similar modal energy content, and confirmed from the examination of the corresponding spatial eigenmodes and identical spectra of temporal coefficients. The occurrence of paired modes is a characteristic feature of POD modes in flows containing periodic structures [68]. For the unconfined case the first mode pair contains 44.6% of the total energy in the upstream FOV ($0.5h \leq x/h \leq 5.5h$). In contrast, over the same spatial extent, the first mode pair for the CR = 7 and CR = 5 cases contain 34.4% and 29.8% of the total energy, respectively. The second mode pair for

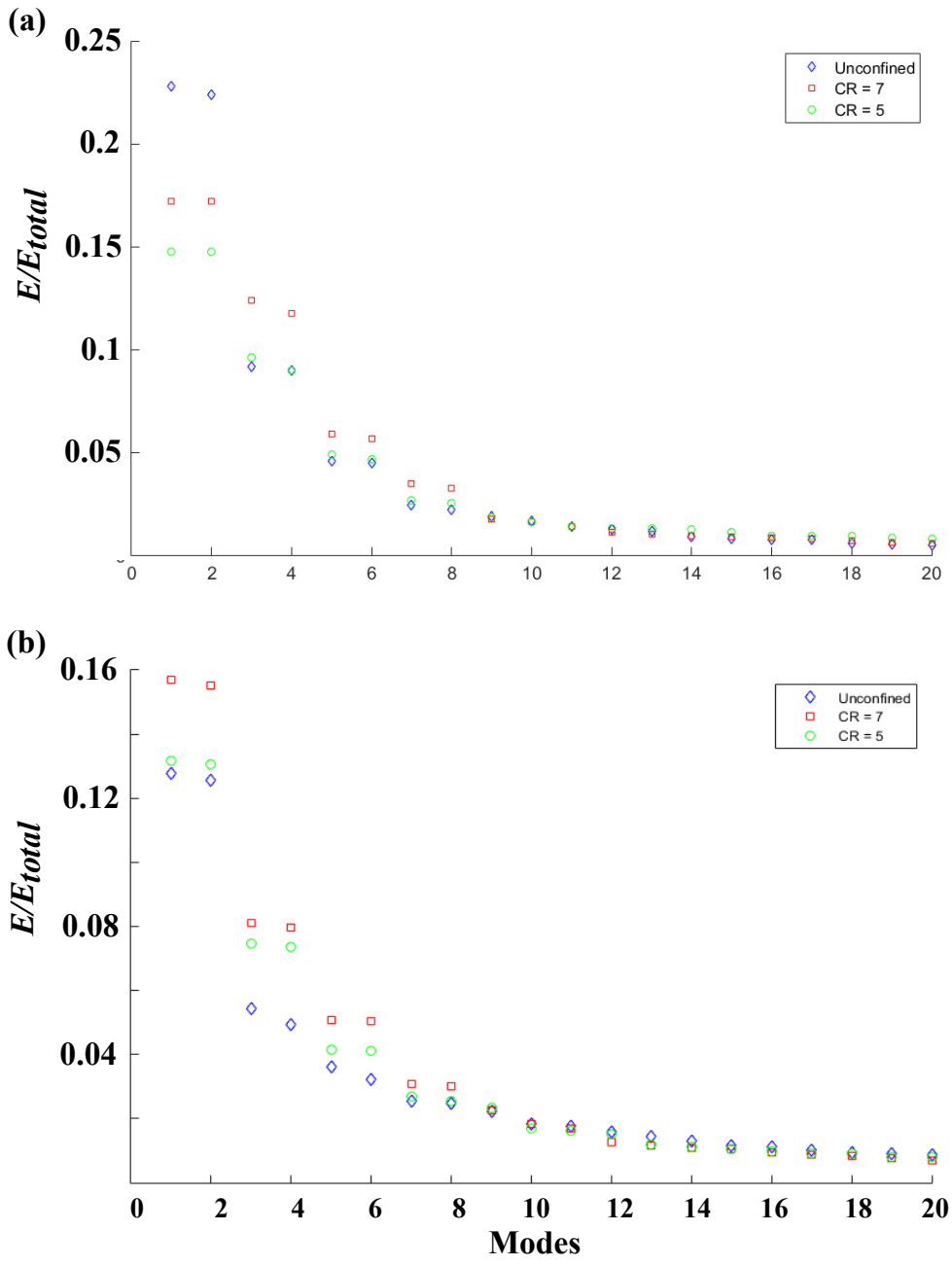

Figure 4.16: Relative energy of modes for (a) Upstream and (b) Downstream FOV

the unconfined case in the upstream FOV contains only 18.2% of the total energy while the corresponding mode pair for CR = 7 and CR = 5 cases contain 24.8% and 20.2% of the total energy, respectively. Thus, in the upstream FOV, the first mode pair for the confined cases has a smaller proportion of total energy than the unconfined case. In contrast, the second, third, and fourth mode pairs for the confined cases contain a greater proportion of the total energy than the corresponding mode pairs for the unconfined case. In the downstream FOV, the four most energetic mode pairs for the confined cases have a greater proportion of energy than, the unconfined case.

The streamnormal components of the eigenmodes (ψ_v) corresponding to the first and third modes are vizualised in Figures 4.17 and 4.18, respectively. Each mode appearing in a mode pair shows similar topological characteristics shifted by a phase angle of $\pi/2$. Therefore only one eigenmode from each of the first and second mode pair are shown for each FOV. The contour plots of ψ_v allows the estimation of streamwise wavelengths (λ_x) corresponding to the most energetic modes. The values of these wavelengths are summarized in Table 4.3. For the unconfined case, in the upstream FOV, mode 1 shows $\lambda_x = 3.24h$ while the confined cases, in the same FOV, shows a mode 1 wavelength of $\lambda_x = 1.07h$, this indicates that the structures corresponding to the most energetic mode in the unconfined case in FOV1, are the structures that have undergone two pairings, while for the confined cases mode 1 represents the primary structures. In the downstream FOV, the wavelengths of the most energetic modes increase for all three cases reflecting structures are formed as a result of further pairings. The most energetic mode for the unconfined case corresponds to structures that have undergone two complete pairings and have a wavelength of almost $\lambda_x = 4h$. The corresponding mode for the confined cases has a wavelength of $\lambda_x = 2.5h$ which is indicative of the fact that it represents "triplet" structures discussed earlier.

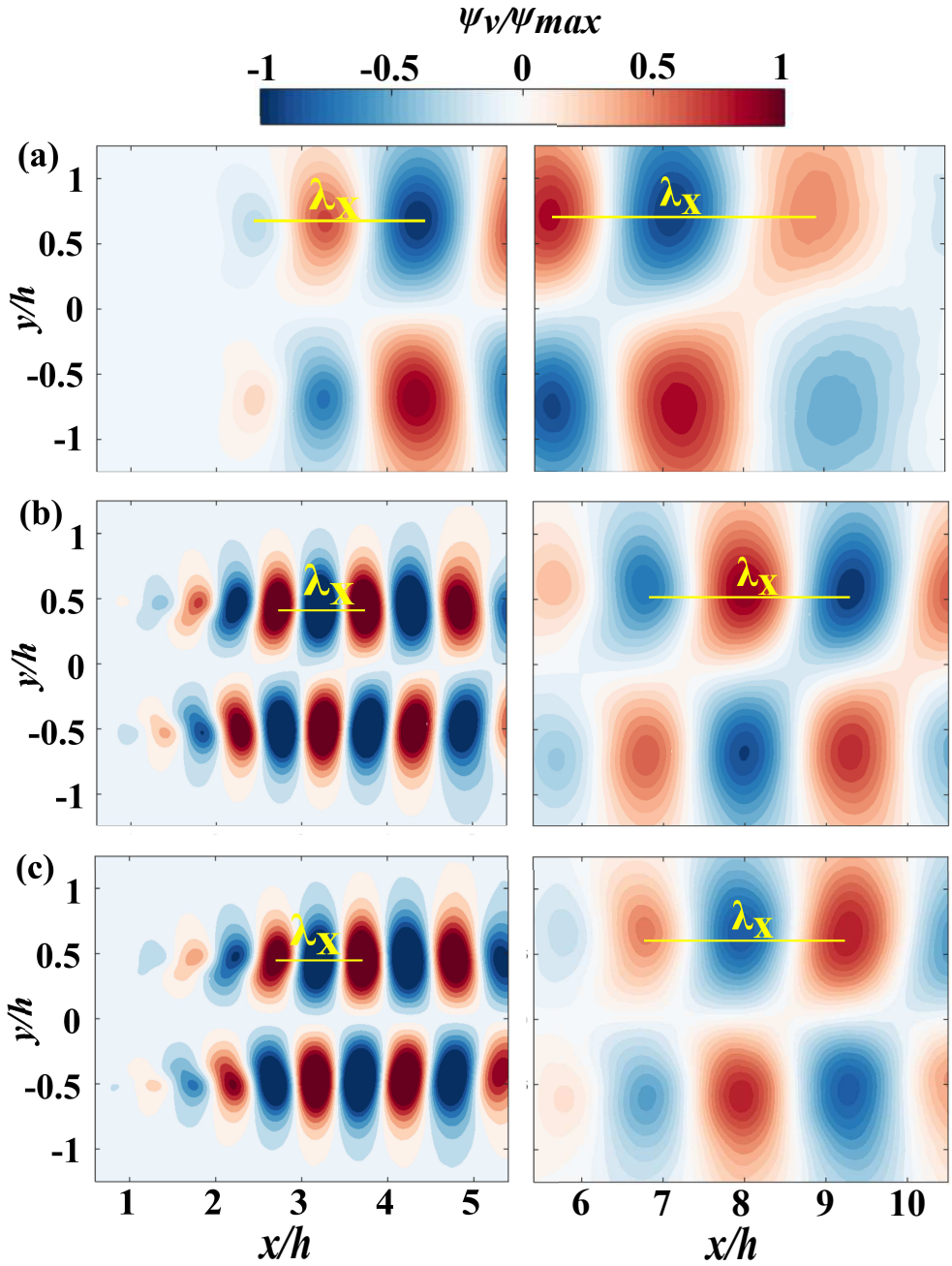

Figure 4.17: Contours of normalised ψ_v for Mode 1 for (a) Unconfined, (b) CR = 7, and (c) CR = 5

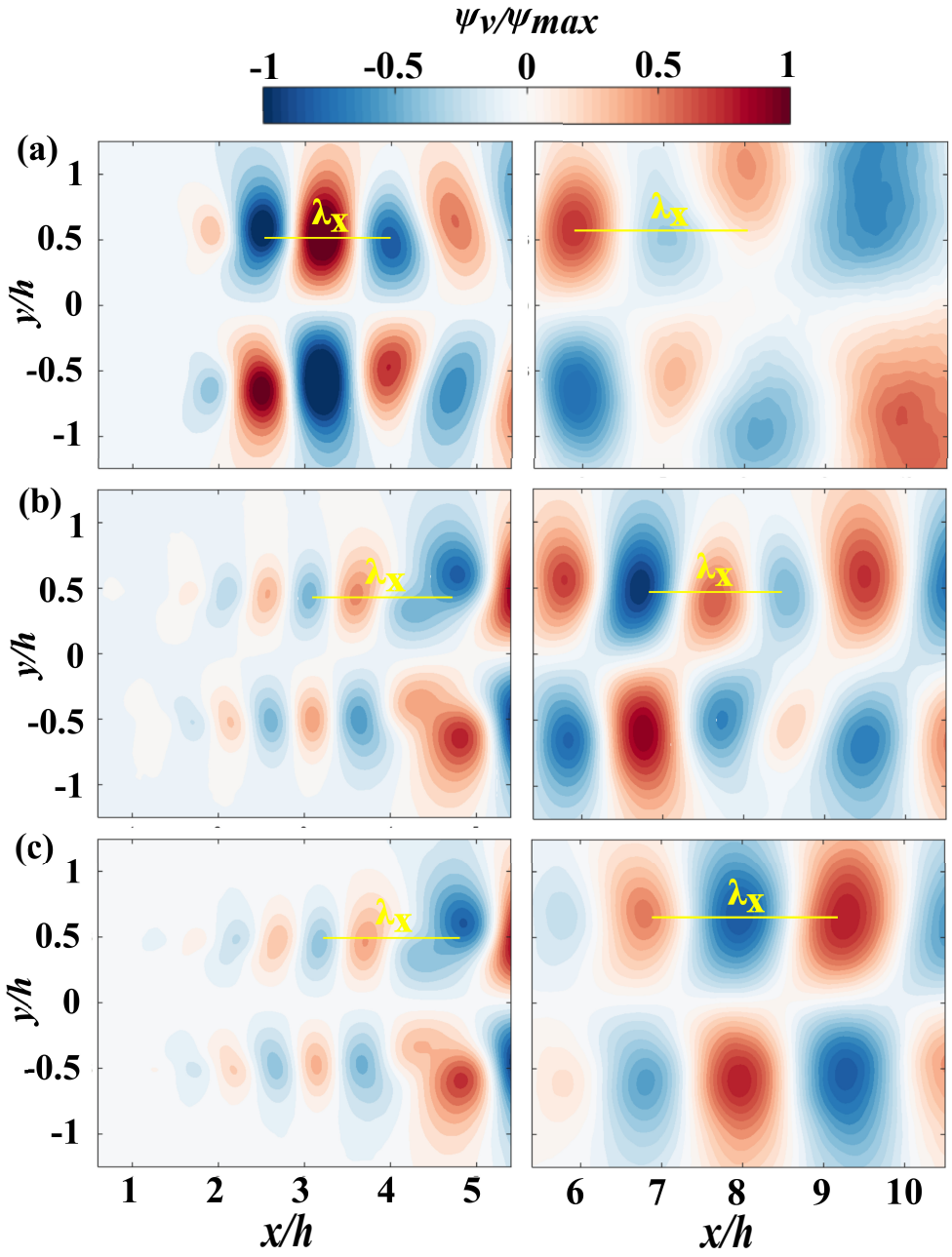

Figure 4.18: Contours of normalised ψ_v for Mode 3 for (a) Unconfined, (b) CR = 7, and (c) CR = 5

Case	Mode 1 (FOV1)	Mode 3 (FOV1)	Mode 1 (FOV2)	Mode 3 (FOV2)
Unconfined	3.24h	1.48h	3.98h	2.14h
CR = 7	1.07h	1.86h	2.57h	1.88h
CR = 5	1.07h	1.86h	2.57h	1.88h

Table 4.3: Streamwise wavelength estimates from streamnormal POD modes.

The extraction of the temporal coefficients allows the study of their power spectral densities. Each mode in a pair showed similar spectra, and therefore, the spectral characteristics of modes 1 and 3, the two most energetic modes with unique spectral properties, are shown in Figure 4.19. For the unconfined case, in the upstream FOV, the spectrum for mode 1 shows high energy content around the second subharmonic of the vortex shedding frequency ($St_0/4$), where $St_0 = 0.67$, confirming the structures represented by this mode are vortices which have undergone two complete pairings. The frequency corresponding to the spectral peak for mode 1 remains unchanged in the downstream FOV. The spectrum for mode 3 shows two broad peaks containing frequencies in the range of $St_0/2$ to $0.4St_0$ corresponding to the paired and "triplet" structures in the flow. This indicates that even in the unconfined case some "triplet" structures might occur. However, they seem to be extremely rare events. In the downstream FOV, the spectral energy for mode 1 is concentrated around a range of frequencies centred at $St_0/4$ and a secondary peak is observed at $St_0/2$ corresponding to structures that have undergone 1 - 3 pairings. Mode 3 shows a peak at a lower Strouhal number than the peak for mode 1. The spectra of the temporal coefficients of the two confined cases show similar characteristics but differ from the unconfined results. In the upstream FOV, the spectrum of mode 1 shows a peak at St_0 indicating that this mode corresponds to the structures formed from the initial roll up of the shear layer. In the downstream FOV, for mode 1, the spectral energy is concentrated around $0.4St_0$ which corresponds to the "triplet" pairing event. The spectrum for

mode 3, in the upstream FOV, has a broad peak centred at $St_0/2$ corresponding to paired structures, while in the downstream FOV, the spectrum for mode 3 show a double peak centred at $St_0/2$ and $St_0/4$ respectively, indicating that this mode has contributions from structures that have undergone singe and double pairings.

The quantitative data obtained from the POD analysis provides insights to the differences in the dynamics of coherent structures between the unconfined and confined cases and the contribution of these structures to the most velocity fluctuations in the flow. For unconfined jets the most energetic mode in the upstream FOV (mode 1) corresponds to structures that have undergone two complete pairings. Conversely, for confined cases, over the same spatial extent downstream of the jet exit, the most energetic mode corresponds to the primary structures shed from the initial roll-up of the shear layer. Farther downstream, in the second FOV for the unconfined flow, the most energetic mode corresponds to vortices formed from two pairings. In contrast, the most energetic mode in the same FOV for the confined cases correspond to the "triplet" structures discussed earlier. This solidfies the argument that while in the unconfined cases the coherent structures undergo multiple pairings within a distance of $x/h = 5.5$, for the unconfined cases this process is delayed until further downstream.

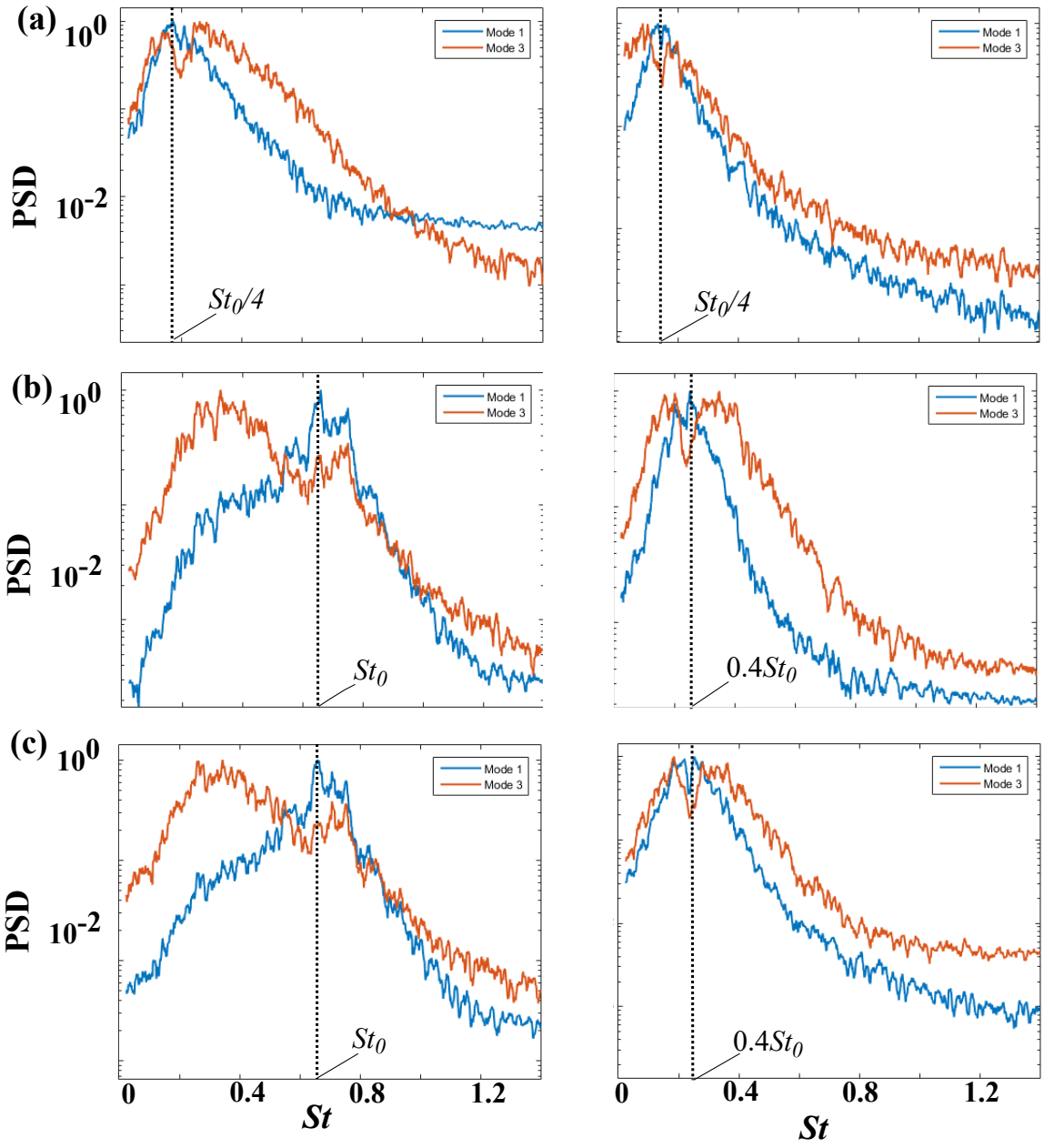

Figure 4.19: PSD of temporal coefficients of POD. (a) Unconfined, (b) CR = 7, and (c) CR = 5.

Chapter 5

Conclusions

The flow development of a planar jet which is confined in the streamnormal direction is studied at two different confinement ratios (CR) of 7 and 5, respectively. The effects of confinement on the flow field and the dynamics of coherent structures are compared to those of a baseline unconfined jet. All experiments are performed at the same Reynolds number of Re = 3800. Quantitative measurements of the velocity fields are obtained using time-resolved planar PIV. The flow-field is captured up to 10.5 jet-slot heights from the jet exit.

Time averaged statistics show that the addition of confinement causes the development of a significant co-flow as compared to the unconfined case. The potential core length is shown to increase and the jet spread rate significantly decreases in the confined cases. The time-averaged turbulence statistics show a decrease in magnitudes of fluctuations for the confined cases at the same locations downstream of the jet exit, in the shear layer, as compared to the unconfined case.

Downstream of the jet exit, the shear layers of the planar jet roll up to form coherent

structures. These structures convect downstream and pair up due to mutual induction. For the unconfined case, the structures are observed to undergo multiple pairings and vortex breakdown is observed downstream of 7 slot heights. For the confined cases, the structures are observed to undergo fewer consecutive pairings than in the unconfined case over an equivalent streamwise distance and vortex breakdown is not observed at up to 10.5 jet slot heights downstream. The passage frequency of the initially shed vortices remain relatively unchanged for the unconfined and confined cases at $St_0 = 0.67$. Not all structures in confined cases undergo pairing and this leads to the formation of a "triplet" structure. This is formed from the successive pairing of a paired structure and a primary structure and has a passage frequency of $0.4St_0$. The addition of confinement causes an increase in the convective velocity of the coherent structures in the shear layer from $0.57U_0$ to $0.64U_0$. The wavelengths of the primary structures are also observed to increase from $0.8h$ in the unconfined case to $1.1h$ in the confined cases.

Downstream of the jet exit, the perturbations in the shear layer are seen to grow exponentially, saturate and then decay. The fluctuations associated with the passage frequency primary structures (St_0), for the unconfined case, saturate at $1.8h$. For the confined cases, the growth rate of these fluctuations are lower, and they saturate at $3.1h$ and $3.7h$ for the CR = 7 and CR = 5 cases, respectively. The location of saturation of these fluctuations also corresponds to the onset of growth of fluctuations associated with the subharmonic ($St_0/2$) which is associated with the structures formed from the pairing of the primary vortices. Therefore, for the confined cases, the location of the first pairing of primary vortices is shifted further downstream. The growth rate of the fluctuations corresponding to the subharmonic is also lower for confined cases than the unconfined case.

Proper Orthogonal Decomposition (POD) analysis shows that, within the first 5.5 jet slot heights downstream of the jet exit, the eight most energetic modes are paired, as

indicated by the equivalent relative energy and similar spectral content of temporal coefficients. For the unconfined case, the most energetic mode pair has a streamwise wavelength of $3.24h$, and the power spectrum of temporal coefficients associated with this mode pair shows a concentration of energy at the second subharmonic of the primary vortex shedding frequency ($St_0/4$). This indicates that this mode corresponds to structures that have undergone two complete pairings. In contrast, in the confined cases, over the same spatial extent downstream, the most energetic mode pair has streamwise wavelength equal to $1.07h$, and the power spectrum of their temporal coefficients shows a peak at the primary vortex shedding frequency (St_0), thus indicating that this mode pair is associated with the primary vortices formed from the roll-up of the shear layer. Farther downstream, the most energetic mode pair for the unconfined case, corresponds to structures having undergone two complete pairings with a streamwise wavelength of $3.98h$. For the confined cases, the most energetic mode pair in the downstream FOV is representative of a "triplet" structure with a streamwise wavelength of $2.57h$ and the spectrum of the temporal coefficients associated with this mode shows a peak at $0.4St_0$. This corresponds to earlier observations regarding the structure formed from the merging of a paired and a primary vortex, which is observed only in the confined cases.

Chapter 6

Recommendations

The results of the present work and the conclusions drawn from them lead to some additional questions that may serve as topics for studies in the future. The following recommendations are therefore made for future work:

- Expand the parameter space in terms of higher confinement ratios in order to better determine the trends with respect to the growth rate of fluctuations in the shear layer, convective velocity, and wavelengths of coherent structures with increasing confinement.
- Include fields of view with greater extents in the streamnormal direction. This would allow the measurement of parts of the flow field where the boundary layer developing over the confinement walls interacts with the spreading shear layers and would thereby allow the study of the effects of this interaction on the coherent structures, in the confined cases.
- Implement vortex tracking in order to determine the convective velocities of individual classes of structures (primary, paired and "triplet" structures). The present use

of determining velocities from a convective ridge on a frequency-wavenumber plot is only applicable for average velocities. Vortex tracking would allow for determination of the velocities individually for each kind of structure (primary, paired, and triplet) over both Fields of View. This would provide information about changes in convective velocities for each kind of vortex over different cases and provide additional insight regarding the behavior of vortices in space and time.

- Perform wavelet analysis in order to determine the time variation of frequencies at various regions of interest in the flow field. While the present study has quantified variation in spatial locations of pairing with confinement, wavelet analysis would allow the quantification of the number of times pairing and "triplet" events would occur over a given observation window and provide additional insight regarding the effects of confinement on these events.

- Extend the Fields of View further downstream, in order to study the effects of the recirculation bubble, which occurs under certain conditions in confined jet flows, on the coherent structures.

- Perform a similar study in the case where the confinement box expands in internal area downstream of the jet exit instead of being rectangular.

References

[1] A. Craya and R. Curtet, "On the spreading of a confined jet," *CR Academy of Science Paris*, vol. 241, no. 1, pp. 621–622, 1955.

[2] R. Curtet, "Confined jets and recirculation phenomena with cold air," *Combustion and Flame*, vol. 2, no. 4, pp. 383–411, 1958.

[3] W. Quinn, "Streamwise evolution of a square jet cross section," *AIAA Journal*, vol. 30, no. 12, pp. 2852–2857, 1992.

[4] M. Stephane, S. Camille, and P. Michel, "Parametric analysis of the impinging plane air jet on a variable scaled-down model," in *Proc: ASME/JSME Fluids Engineering Division Summer Meeting, F-227, Boston, Massachusetts*, 2000.

[5] B. Moshfegh, M. Sandberg, and S. Amiri, "Spreading of turbulent warm/cold plane air jet in a well-insulated room," *Over the Internet: http://www. hig. se/tinst/forskning/em/spreading-of-turbulent. htm, Supported by: University of Gavle and KK-Foundation*, 2004.

[6] D. Liberzon and H. Fernando, "Pressure distribution in confined jet flow," *Journal of Fluids Engineering*, vol. 136, no. 3, p. 031202, 2014.

[7] M.-S. Cha and S.-H. Chung, "Characteristics of lifted flames in nonpremixed turbulent confined jets," in *Symposium (International) on Combustion*, vol. 26, pp. 121–128, Elsevier, 1996.

[8] K. Sodjavi, B. Montagné, P. Bragança, A. Meslem, P. Byrne, C. Degouet, and V. Sobolik, "PIV and electrodiffusion diagnostics of flow field, wall shear stress and mass transfer beneath three round submerged impinging jets," *Experimental Thermal and Fluid Science*, vol. 70, pp. 417–436, 2016.

[9] S. C. Crow and F. Champagne, "Orderly structure in jet turbulence," *Journal of Fluid Mechanics*, vol. 48, no. 3, pp. 547–591, 1971.

[10] C. D. Winant and F. K. Browand, "Vortex pairing: the mechanism of turbulent mixing-layer growth at moderate Reynolds number," *Journal of Fluid Mechanics*, vol. 63, no. 2, pp. 237–255, 1974.

[11] A. F. Hussain, "Coherent structures reality and myth," *The Physics of Fluids*, vol. 26, no. 10, pp. 2816–2850, 1983.

[12] G. S. Beavers and T. A. Wilson, "Vortex growth in jets," *Journal of Fluid Mechanics*, vol. 44, no. 1, pp. 97–112, 1970.

[13] F. Gori, I. Petracci, and M. Angelino, "Influence of the Reynolds number on the instant flow evolution of a turbulent rectangular free jet of air," *International Journal of Heat and Fluid Flow*, vol. 50, pp. 386–401, 2014.

[14] J. Westerweel, G. E. Elsinga, and R. J. Adrian, "Particle image velocimetry for complex and turbulent flows," *Annual Review of Fluid Mechanics*, vol. 45, pp. 409–436, 2013.

[15] E. Razinsky and J. Brighton, "Confined jet mixing for nonseparating conditions," *Journal of Basic Engineering*, vol. 93, no. 3, pp. 333–347, 1971.

[16] R. A. Antonia and R. W. Bilger, "An experimental investigation of an axisymmetric jet in a co-flowing air stream," *Journal of Fluid Mechanics*, vol. 61, no. 4, p. 805822, 1973.

[17] A. Yule and M. Damou, "Investigations of ducted jets," *Experimental Thermal and Fluid Science*, vol. 4, no. 4, pp. 469–490, 1991.

[18] B. Kong, M. Olsen, R. Fox, and J. Hill, "Predictive capability of large eddy simulation for point-wise and spatial turbulence statistics in a confined rectangular jet," *Chemical Engineering Science*, vol. 69, no. 1, pp. 240–256, 2012.

[19] I. Lee, *An Experimental and Numerical Study of Confined Non-reacting and Reacting Turbulent Jets to Facilitate Homogeneous Combustion in Industrial Furnaces.* PhD thesis, University of Michigan, 2015.

[20] A. Yule, "Large-scale structure in the mixing layer of a round jet," *Journal of Fluid Mechanics*, vol. 89, no. 3, pp. 413–432, 1978.

[21] A. F. Hussain and K. Zaman, "The preferred modeof the axisymmetric jet," *Journal of Fluid Mechanics*, vol. 110, pp. 39–71, 1981.

[22] J. N. Livingood and P. Hrycak, "Impingement heat transfer from turbulent air jets to flat plates: a literature survey," *NASA*, 1973.

[23] R. Deo, *Experimental investigations of the influence of Reynolds number and boundary conditions on a plane air jet.* PhD thesis, The University of Adelaide, 2005.

[24] R. C. Deo, G. J. Nathan, and J. Mi, "Comparison of turbulent jets issuing from rectangular nozzles with and without sidewalls," *Experimental Thermal and Fluid Science*, vol. 32, no. 2, pp. 596–606, 2007.

[25] R. C. Deo, J. Mi, and G. J. Nathan, "The influence of Reynolds number on a plane jet," *Physics of Fluids*, vol. 20, no. 7, p. 075108, 2008.

[26] J. Mi, G. Nathan, and D. Nobes, "Mixing characteristics of axisymmetric free jets from a contoured nozzle, an orifice plate and a pipe," *Journal of Fluids Engineering*, vol. 123, no. 4, pp. 878–883, 2001.

[27] C.-M. Ho and P. Huerre, "Perturbed free shear layers," *Annual Review of Fluid Mechanics*, vol. 16, no. 1, pp. 365–422, 1984.

[28] R. Antonia, L. Browne, S. Rajagopalan, and A. Chambers, "On the organized motion of a turbulent plane jet," *Journal of Fluid Mechanics*, vol. 134, pp. 49–66, 1983.

[29] R. C. Deo, J. Mi, and G. J. Nathan, "The influence of Reynolds number on a plane jet," *Physics of Fluids*, vol. 20, no. 7, p. 075108, 2008.

[30] V. Goldschmidt, M. Young, and E. Ott, "Turbulent convective velocities (broadband and wavenumber dependent) in a plane jet," *Journal of Fluid Mechanics*, vol. 105, pp. 327–345, 1981.

[31] R. Antonia, A. Chambers, D. Britz, and L. Browne, "Organized structures in a turbulent plane jet: topology and contribution to momentum and heat transport," *Journal of Fluid Mechanics*, vol. 172, pp. 211–229, 1986.

[32] F. Thomas and E. Brehob, "An investigation of large-scale structure in the similarity region of a two-dimensional turbulent jet," *Physics of Fluids*, vol. 29, no. 6, pp. 1788–1795, 1986.

[33] H. Sato, "The stability and transition of a two-dimensional jet," *Journal of Fluid Mechanics*, vol. 7, no. 1, pp. 53–80, 1960.

[34] D. O. Rockwell and W. O. Niccolls, "Natural breakdown of planar jets," *Journal of Basic Engineering*, vol. 94, no. 4, pp. 720–728, 1972.

[35] A. Chambers, R. Antonia, and L. Browne, "Effect of symmetry and asymmetry of turbulent structures on the interaction region of a plane jet," *Experiments in Fluids*, vol. 3, no. 6, pp. 343–348, 1985.

[36] F. Thomas and K. Prakash, "An experimental investigation of the natural transition of an untuned planar jet," *Physics of Fluids A: Fluid Dynamics*, vol. 3, no. 1, pp. 90–105, 1991.

[37] A. K. M. F. Hussain, "Coherent structures and turbulence," *Journal of Fluid Mechanics*, vol. 173, p. 303356, 1986.

[38] I. Namer and M. Ötügen, "Velocity measurements in a plane turbulent air jet at moderate Reynolds numbers," *Experiments in Fluids*, vol. 6, no. 6, pp. 387–399, 1988.

[39] I. Wygnanski and H. Fiedler, "Some measurements in the self-preserving jet," *Journal of Fluid Mechanics*, vol. 38, no. 3, pp. 577–612, 1969.

[40] J. T. C. Liu, "Coherent structures in transitional and turbulent free shear flows," *Annual Review of Fluid Mechanics*, vol. 21, no. 1, pp. 285–315, 1989.

[41] A. Michalke, "On the inviscid instability of the hyperbolictangent velocity profile," *Journal of Fluid Mechanics*, vol. 19, no. 4, pp. 543–556, 1964.

[42] P. A. Monkewitz and P. Huerre, "Influence of the velocity ratio on the spatial instability of mixing layers," *Physics of Fluids*, vol. 25, no. 7, pp. 1137–1143, 1982.

[43] C.-M. Ho and L.-S. Huang, "Subharmonics and vortex merging in mixing layers," *Journal of Fluid Mechanics*, vol. 119, pp. 443–473, 1982.

[44] P. A. Monkewitz, "Subharmonic resonance, pairing and shredding in the mixing layer," *Journal of Fluid Mechanics*, vol. 188, pp. 223–252, 1988.

[45] F.-B. Hsiao and J.-M. Huang, "On the evolution of instabilities in the near field of a plane jet," *Physics of Fluids A: Fluid Dynamics*, vol. 2, no. 3, pp. 400–412, 1990.

[46] M. V. Shestakov, V. M. Dulin, M. P. Tokarev, D. P. Sikovsky, and D. M. Markovich, "PIV study of large-scale flow organisation in slot jets," *International Journal of Heat and Fluid Flow*, vol. 51, pp. 335–352, 2015.

[47] S. Voropayev, X. Sanchez, C. Nath, S. Webb, and H. J. S. Fernando, "Evolution of a confined turbulent jet in a long cylindrical cavity: homogeneous fluids," *Physics of Fluids*, vol. 23, no. 11, p. 115106, 2011.

[48] J. R. Landel, C. Caulfield, and A. W. Woods, "Streamwise dispersion and mixing in quasi-two-dimensional steady turbulent jets," *Journal of Fluid Mechanics*, vol. 711, pp. 212–258, 2012.

[49] V. H. Chu and W. D. Baines, "Entrainment by buoyant jet between confined walls," *Journal of Hydraulic Engineering*, vol. 115, no. 4, pp. 475–492, 1989.

[50] P. G. Hill, "Turbulent jets in ducted streams," *Journal of Fluid Mechanics*, vol. 22, no. 1, pp. 161–186, 1965.

[51] M. Habib and J. Whitelaw, "Velocity characteristics of a confined coaxial jet," *Journal of Fluids Engineering*, vol. 101, no. 4, pp. 521–529, 1979.

[52] T. Nickels and A. Perry, "An experimental and theoretical study of the turbulent coflowing jet," *Journal of Fluid Mechanics*, vol. 309, pp. 157–182, 1996.

[53] B. Kong, M. Olsen, R. Fox, and J. Hill, "Population, characteristics and kinematics of vortices in a confined rectangular jet with a co-flow," *Experiments in Fluids*, vol. 50, no. 6, pp. 1473–1493, 2011.

[54] A. Michalke, "On the influence of a wake on the inviscid instability of a circular jet with external flow," *European Journal of Mechanics. B, Fluids*, vol. 12, no. 5, pp. 579–595, 1993.

[55] A. Talamelli and I. Gavarini, "Linear instability characteristics of incompressible coaxial jets," *Flow, Turbulence and Combustion*, vol. 76, no. 3, pp. 221–240, 2006.

[56] A. Segalini and A. Talamelli, "Experimental analysis of dominant instabilities in coaxial jets," *Physics of Fluids*, vol. 23, no. 2, p. 024103, 2011.

[57] S. Pieris, "Experimental investigation of a normally impinging planar jet," Master's thesis, University of Waterloo, 2017.

[58] R. J. Adrian and J. Westerweel, *Particle image velocimetry*. No. 30, Cambridge University Press, 2011.

[59] F. Thomas and V. Goldschmidt, "Structural characteristics of a developing turbulent planar jet," *Journal of Fluid Mechanics*, vol. 163, pp. 227–256, 1986.

[60] L. Browne, R. Antonia, and A. Chambers, "The interaction region of a turbulent plane jet," *Journal of Fluid Mechanics*, vol. 149, pp. 355–373, 1984.

[61] M. Raffel, C. E. Willert, F. Scarano, C. J. Kähler, S. T. Wereley, and J. Kompenhans, *Particle image velocimetry: a practical guide*. Springer, 2018.

[62] J. Jeong and F. Hussain, "On the identification of a vortex," *Journal of Fluid Mechanics*, vol. 285, pp. 69–94, 1995.

[63] F. F. Grinstein, "Vortex dynamics and entrainment in rectangular free jets," *Journal of Fluid Mechanics*, vol. 437, pp. 69–101, 2001.

[64] J. Oler and V. Goldschmidt, "A vortex-street model of the flow in the similarity region of a two-dimensional free turbulent jet," *Journal of Fluid Mechanics*, vol. 123, pp. 523–535, 1982.

[65] M. S. Howe, *Acoustics of fluid-structure interactions*. Cambridge University Press, 1998.

[66] R. Handler, G. Smith, and R. Leighton, "The thermal structure of an air–water interface at low wind speeds," *Tellus A*, vol. 53, no. 2, pp. 233–244, 2001.

[67] M. Wheeler and G. N. Kiladis, "Convectively coupled equatorial waves: Analysis of clouds and temperature in the wavenumber–frequency domain," *Journal of the Atmospheric Sciences*, vol. 56, no. 3, pp. 374–399, 1999.

[68] K. Taira, S. L. Brunton, S. T. Dawson, C. W. Rowley, T. Colonius, B. J. McKeon, O. T. Schmidt, S. Gordeyev, V. Theofilis, and L. S. Ukeiley, "Modal analysis of fluid flows: An overview," *AIAA Journal*, pp. 4013–4041, 2017.

[69] J. L. Lumley, "The structure of inhomogeneous turbulent flows," *Atmospheric turbulence and radio wave propagation*, 1967.

[70] G. Berkooz, P. Holmes, and J. L. Lumley, "The proper orthogonal decomposition in the analysis of turbulent flows," *Annual Review of Fluid Mechanics*, vol. 25, no. 1, pp. 539–575, 1993.

[71] R. J. Moffat, "Describing the uncertainties in experimental results," *Experimental Thermal and Fluid Science*, vol. 1, no. 1, pp. 3–17, 1988.

[72] A. Sciacchitano, B. Wieneke, and F. Scarano, "PIV uncertainty quantification by image matching," *Measurement Science and Technology*, vol. 24, no. 4, p. 045302, 2013.

[73] A. Sciacchitano and B. Wieneke, "Piv uncertainty propagation," *Measurement Science and Technology*, vol. 27, no. 8, p. 084006, 2016.

[74] M. Olsson and L. Fuchs, "Large eddy simulations of a forced semiconfined circular impinging jet," *Physics of Fluids*, vol. 10, no. 2, pp. 476–486, 1998.

APPENDICES

Appendix A

Uncertainty Analysis

A.1 Experimental Uncertainty

The determination of uncertainty is important for the interpretation of results in order to gauge their significance. For the present work the methodology of Moffat [71] has been utilised to determine the total uncertainty associated with a particular quantity ϵ_t due to n as:

$$\epsilon_t = \left(\sum_{n=i}^{n} \epsilon_i^2 \right)^{0.5} \tag{A.1}$$

For a derived quantity $y = f(x_1, x_2, ..., x_n)$, where $x_1, x_2....., x_n$, are the measured quantities and y is the derived quantity, the uncertainty is determined as

$$\epsilon_t = \left[\frac{\partial f}{\partial x_1}\epsilon_{x1} + \frac{\partial f}{\partial x_2}\epsilon_{x2} + ... + \frac{\partial f}{\partial x_n}\epsilon_{xn} \right]^{0.5} \tag{A.2}$$

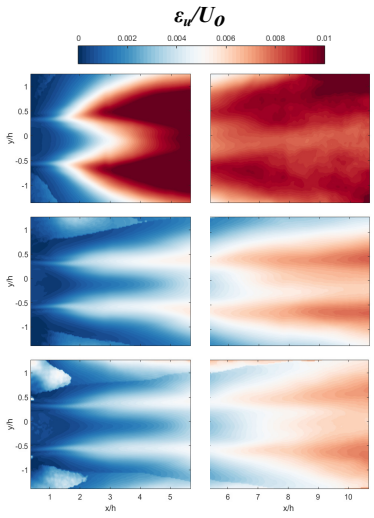

Figure A.1: Contours of random PIV error for all 3 cases over both FOVs of normalised Velocity magnitude (U)

The uncertainty of all results presented in this work is calculated over a 95% confidence interval.

Uncertainty estimation of PIV is a difficult process primarily due to the large number of factors which contribute to the complex process of measuring the velocity field. For the present case the uncertainty is estimated using the particle disparity method [72]. This is an *a posteriori* method which uses the particle images to estimate the uncertainty in the instantaneous, mean and fluctuating velocity fields. This error arises from various factors including out-of-plane particle motions, non-uniform seeding, lighting disparities and high velocity gradients.

Figure A.1 shows the random error estimates in the velocity magnitude and the streamwise and streamnormal velocity fluctuations over both Fields of View (FOVs) for all three cases. Overall the uncertainty estimates are the highest in the unconfined cases. For the velocity magnitude a maximum error of $\epsilon/U_0 = 1\%$ is observed in the shear layer due to the sharp velocity gradients experienced there. Additionally, for all three cases the uncertainty

Case	ϵ_{urms}/U_0	ϵ_{vrms}/U_0	ϵ_{RSS}/U_0^2
Unconfined	0.55%	0.69%	0.11%
CR = 7	0.27%	0.41%	0.07%
CR = 5	0.25%	0.38%	0.06%

Table A.1: Uncertainty estimates for turbulence quantities

estimates are higher in the downstream FOV than the corresponding upstream FOV.

The uncertainties related to the statistical turbulence quantities of u_{rms} and v_{rms} are calculated using the procedure given in Sciacchitano and Wienke [73] where the the uncertainty related to any given turbulence quantity ϵ_t is computed according to the equation

$$\epsilon_t = R_t \sqrt{\frac{2}{N}} \tag{A.3}$$

where R_t is the turbulence quantity in question and N is the number of uncorrelated time samples. The uncertainty related to the RSS is calculated using the following equation also obtained from Sciacchitano and Wienke [73].

$$U_{RSS} = \sigma_u \sigma_v \sqrt{\frac{1+\rho_{uv}^2}{N-1}} \tag{A.4}$$

where σ_u and σ_v are the standard deviations of the u and v fields and ρ_{uv} is a correlation coefficient. Using the above methods the estimates for the maximum uncertainties in u_{rms},v_{rms} and RSS for all three cases are given in Table A.1

The primary quantity related to the dynamics of coherent structures is the frequency spectra of $v^{'}$ which educes the passage frequency of coherent structures. The spectra are calculated using Welch's averaged modified spectrogram approach [74]. The window size utilised is 1024 and this results in a frequency resolution of $\Delta f = 3$ Hz, which results in

a Strouhal number resolution of $St = 0.006$ for all cases. The uncertainty associated with any particular frequency is half the resolution resulting in a relative error of $\epsilon_{St}/St_0 = \pm 0.4\%$.

The convective velocities of the coherent structures are determined from a linear fit to the points of maximum energy of the 2D PSD for all cases. The convective velocities in these cases are therefore a function of the Root Mean Square Error (RMSE) of the fit and frequency and wavenumber resolutions of the frequency wavenumber spectra. The frequency resolution is identical to the 1D spectra and the uncertainty therefore ranges from $\pm 0.26\%$ to $\pm 0.62\%$. The wavenumber resolution is $1.1/\Delta h$ and the uncertainty related to the wavenumber is $\pm 0.6\% \leq \epsilon/\lambda_o \leq \pm 1.75\%$. The uncertainty in the convective velocities due to the quality of the linear fit ranges from $\pm 7.2\% \leq \epsilon/U_0 \leq \pm 15\%$. Since the contribution from the RMSE of the fit is far larger than from frequency and wavenumber resolution error, they may be effectively ignored.